

Ab-initio Insights on the Fermiology of d^1 Transition metals in Honeycomb lattice : Hierarchy of hopping pathways and spin-orbit coupling

Manoj Gupta^{a,1,*}, Basudeb Mondal^{a,2,†}, Subhro Bhattacharjee^{2,‡} and Tanusri Saha Dasgupta^{1,§}

¹*Department of Condensed Matter Physics and Materials Science,*

S. N. Bose National Centre for Basic Sciences, Kolkata 700098, India

²*International Centre for Theoretical Sciences, Tata Institute of Fundamental Research, Bengaluru 560 089, India*

(Dated: August 17, 2023)

Motivated by the intriguing suggestion of realizing SU(8) Dirac semi-metal with $J = 3/2$ electrons on a honeycomb lattice, we provide a systematic study of the interplay of various hopping pathways and atomic spin-orbit coupling for the low energy electrons in candidate d^1 transition metal halides MX_3 (M=Ti, Zr, Hf; X=F, Cl, Br). By combining first principle calculations and minimal hopping Hamiltonian, we uncover the role of dominant direct metal-metal hopping on top of indirect metal-halide-metal hopping. This sets up a hierarchy of hopping pathways that centrally modify the SU(8) picture for the above materials. These hopping interactions, along with the spin-orbit coupling, lead to a plethora of exactly compensated metals instead of the SU(8) Dirac semi-metal. Remarkably the same can be understood as descendants of a topological insulator obtained by gapping out the SU(8) Dirac semi-metallic phase. The resultant compensated metals have varied Fermi surface topology and are separated by Lifshitz phase transitions. We discuss the implications of the proximate Lifshitz transition, which may be accessed via strain, in the context of the relevant materials.

I. INTRODUCTION

Electronic phases of transition metal compounds with active d -electrons pose some of the outstanding problems in condensed matter physics. In addition to the well-known effect of electron-electron interactions, in recent times it has been realized that the atomic spin-orbit coupling (SOC) plays an important role in shaping up the structure of the low energy theory of the 4d and 5d transition metal compounds [1, 2]. This provides the scope to study, design and engineer newer platforms of quantum materials supporting novel electronic phases resulting from the interplay of quantum entanglement and symmetries as evidenced in spin-orbit assisted Mott insulators, quantum spin liquids, excitonic magnetism, multipolar orderings, and correlated topological semimetals [3–13].

In particular, for 4d and 5d transition metals in octahedral crystal field and with active t_{2g} orbitals, the strong SOC can split the atomic t_{2g} orbitals into effective higher energy $J = 1/2$ doublet and lower energy $J = 3/2$ quadruplet [3]. In this regard, the physics of the $J = 1/2$ orbitals has been studied extensively [14–16]. In comparison, the compounds with active $J = 3/2$ manifold have received somewhat less attention in spite of the potential to harbor equally or even richer low energy physics.

A potential candidate of expected $J = 3/2$ physics are the transition metal compounds in d^1 electronic state where the t_{2g} orbitals are at $1/6$ th filling. At the strong SOC limit, this leads to an empty $J = 1/2$ manifold, while the $J = 3/2$ orbitals are quarter filled. Among

these compounds, of particular interest to us are layered transition metal (M) halides (X), of general formula MX_3 [17]. The 3^+ transition metal (M) cations in these compounds, in the octahedral setting of 1^{-1} halide anions form honeycomb lattice by edge sharing of MX_6 octahedra. Yamada *et. al.* [18] proposed $ZrCl_3$, a member of these the honeycomb d^1 family, as candidate material exhibiting SU(4) symmetric spin Hamiltonian in the strong coupling limit. Mondal *et. al.* [19] showed that the same can lead to SU(8) Dirac semi-metal (DSM) in the non-interacting limit.

It is to be noted though, the above Hamiltonian(s) were derived under the assumption of infinite SOC limit by projecting to the $J = 3/2$ orbitals, and by considering only indirect hopping, *i.e.* hopping between two M sites via the X. As expected, both of these assumptions are idealized limits vis-a-vis the candidate materials. There are other microscopic energy-scales even at the single electron level – the various hopping amplitudes and non-cubic crystal field splitting – that can compete and change the low energy physics, and hence needs to be understood. While the SU(4) or SU(8) may provide an interesting starting point to capture the intermediate coupling physics in real materials, generically one expects that these other energy scales would reduce the fine tuned SU(4) or SU(8) symmetries for the spin model or the free Dirac theory, respectively. What then is the resultant structure of the low energy theory and the possible electronic phases in this family of materials? More interestingly, the details of these competing microscopic interactions can change across the periodic table even within the same class of MX_3 materials, *e.g.*, in moving from 3d to 4d to 5d transition metal, (M=Ti \rightarrow Zr \rightarrow Hf) and in moving from 2p to 3p to 4p halogen (X=F \rightarrow Cl \rightarrow Br).

In this paper, we present *ab-initio* Density functional theory (DFT) insights into the estimates of the differ-

* *a* The authors contributed equally to this work.;
gpta.mnj@gmail.com

† basudeb.mondal@icts.res.in

‡ subhro@icts.res.in

§ t.sahadasgupta@gmail.com

ent hopping pathways and their effect on the low energy minimal hopping models to reveal a rich structure of the possible phases relevant to MX_3 . Guided by our DFT calculations, we conclude that the low energy fermiology of the electrons requires SOC and a minimal set of four hopping pathways that include two direct dd hopping, $t_{dd\sigma}$ and $t_{dd\pi}$, in addition to two well known [20] indirect ones via the intermediate halide ion, t_{ddm} , $t_{ddm'}$. Across the transition metal series, the hierarchy of direct and indirect hopping shows an interesting evolution with the fluorides being notably different from the chlorides and bromides. This results in a marked deviation from the indirect hopping only model at large SOC.

Starting with the $\text{SU}(8)$ DSM, we provide a controlled understanding of the effect of the other hopping pathways as well as finite SOC. Our DFT results suggest that the largest of the microscopic energy scales is the direct overlap between the transition metals ions, $t_{dd\sigma}$. This, along with finite SOC (λ), allowing for the mixing amongst the different t_{2g} orbitals provide a natural setting to explore the phase diagram in the $t_{dd\sigma}/t_{ddm} - \lambda$ plane around the $\text{SU}(8)$ semi-metal. For chlorides and bromides, the effect of both these perturbations can be understood in terms of gapping out of the $\text{SU}(8)$ Dirac fermions. However, while finite $t_{dd\sigma}$ gives a Z_2 free fermion symmetry protected topological insulator (SPT) [21, 22], finite λ leads to a trivial one with an intervening $\text{SU}(2)$ DSM line separating the two. The primary effect of sub-leading direct and indirect hopping, $t_{dd\pi}$ and $t_{ddm'}$ is to change the details of the band structure around the Fermi level to give rise to particle-hole pockets resulting in a plethora of exactly compensated metals with varied Fermi surface topology. Two characteristic features of the Fermi surfaces relevant for the materials, we note, are – (a) near nesting of different sections of the Fermi pockets, and, (b) proximity to Lifshitz transition which leads to the change in the Fermi surface topology. Remarkably, all these compensated metals are direct descendants of the topological insulator obtained in the $\text{SU}(8)$ limit and carry a non-trivial Z_2 index. Using our ab-initio estimates of the band parameters, we place various materials (chlorides and bromides) on the relevant part of the λ -hopping phase diagram. Interestingly, we find that the chlorides lie close to the phase boundary between the different compensated metals separated by a Lifshitz transition. This opens up the possibility of strain induced Lifshitz transition in monolayer MCl_3 .

The rest of the paper is organized as follows. In Sec. II we introduce the DFT computation details that we use to obtain the electronic band structure, as well as the construction of the low energy Hamiltonian of the compounds. In Sec. III, the crystal structure of the nine compounds, MX_3 where $\text{M}=\text{Ti, Zr, Hf}$ and $\text{X}=\text{F, Cl, Br}$ are discussed. This is followed by the discussion of DFT band structure in Sec. IV and DFT-derived low energy tight binding model in Sec. V. The phase diagrams of the low-energy hopping model in SOC strength and hopping space upon systematic introduction of hopping have

been discussed in subsequent section and sub-sections (cf Sec. VI). This also includes the phase diagram relevant to the discussed chloride and bromide compounds and discussion on the possible Lifshitz transition. We close the result section with a brief overview on the consequences of parameters relevant for fluorides in the $t_{dd\sigma}/t_{ddm} - \lambda$ phase diagram in Sec. VII. In Sec. VIII summary and outlook are presented. Supporting technical details are given in SM [23].

II. METHODS AND COMPUTATIONAL DETAILS

The first-principles DFT calculations were carried out using plane-wave basis and projector augmented-wave potential [24–26], as implemented in Vienna Abinitio Simulation package [27–29]. The Perdew-Burke-Ernzerhof generalized gradient approximation (GGA) [30] was used to approximate the exchange-correlation functional. To check the influence of correlation effect at transition metal site, beyond GGA, GGA+U with supplemented Hubbard U correction was carried out [31]. Further, to handle the van Waals interaction between the layers, dispersion corrected GGA+U+D2 functional was used [32]. The convergence of energies and forces, was ensured by using a plane-wave energy cutoff of 600 eV and BZ sampling with $6 \times 6 \times 6$ Monkhorst-Pack grids. During the structural relaxation, the ions were allowed to move until the atomic forces became lower than 0.0001 eV/Å.

The construction of DFT-derived low energy, few band Hamiltonian in the effective t_{2g} Wannier basis of the transition metal ions was achieved through downfolding technique of integrating out degrees of freedom that are not of interest, starting from the all-orbital DFT bandstructure, calculated in muffin-tin orbital (MTO) basis. The self-consistent potentials required for these calculations, were generated through Stuttgart implementation of Linear-MTO (LMTO) package [33], while the downfolding calculations were performed in Nth-order muffin-tin orbital (NMTO) basis [34]. For muffin-tin orbital calculations, the metal atom-centred MT radii were chosen to be in the range of 1.30-1.53 Å, 1.47-1.66 Å, and 1.44-1.70 Å for Ti, Zr, and Hf, respectively. MT radii of 0.94-0.97 Å, 1.33-1.34 Å, and 1.46-1.48 Å were chosen for halogen atoms, F, Cl, and Br, respectively. The consistency of the results between plane-wave and muffin-tin orbital basis was checked in terms of bandstructure and density of states.

III. CRYSTAL STRUCTURE AND d LEVEL SPLITTING OF THE STUDIED COMPOUNDS

The layered structure of MX_3 compounds comprises of two-dimensional hexagonal nets of MX_3 , van der Waals stacked on each other. Clearly, there can be many vari-

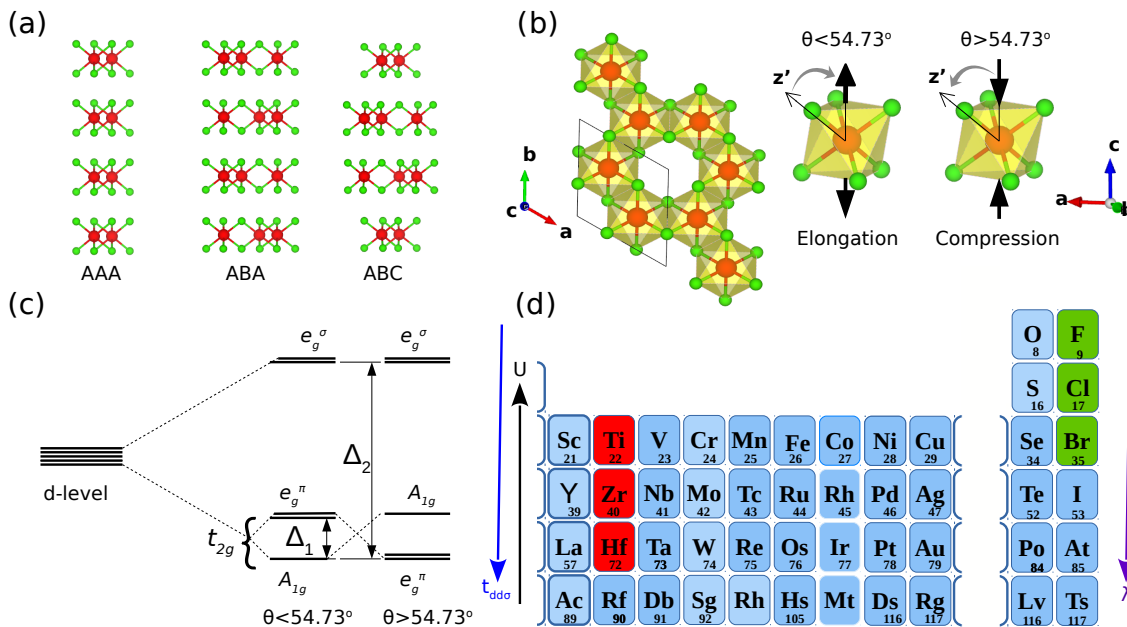


FIG. 1: (a) Different possible stacking of the honeycomb layers in MX_3 family. The M and X atoms are shown as red and green colored balls respectively. (b) Left panel shows the honeycomb layer of M atoms formed by the edge-sharing of MX_6 octahedra. Right panel shows the trigonal distortion of the MX_6 octahedra. (c) The octahedral (Δ_2) and trigonal (Δ_1) crystal field splitting of the d levels of M. (d) The choice of M (marked in red) and X (marked in green) elements of the compounds under study. The variation of the three primary energy scales of the problem – SOC (λ), orbital size dictating the direct metal-metal hopping ($t_{dd\sigma}$) and Coulomb interaction (U) is shown.

ants on the stacking sequence in these layered materials. Due to the weak van der Waals interactions between layers, different stacking sequences result only in small energy differences. For example, TiCl_3 is reported to adopt ABA, AAA, and ABC stacking sequences, as shown in Figure 1(a), with ABA stacking resulting in $\text{P}\bar{3}1\text{c}$ [35], AAA stacking in $\text{P}\bar{3}1\text{m}$ [36], and ABC stacking in $\text{R}\bar{3}$ [35] space groups. Though these polymorphs have different crystal space groups, their in-plane geometry as well as inter-layer distance show little variation, less than 0.2 % for the specific case of TiCl_3 [37]. The weak van der Waals interaction of ~ 1 meV between the layers allows the structure to transform from one stacking type to another, depending on the synthesis procedure. Since we are primarily interested in the in-plane physics of the hexagonal net of d^1 transition metals, for simplicity we will assume AAA stacking of the compounds in the rest of the discussion.

As per the available literature [17] on the layered MX_3 compounds, these compounds have been reported to adopt either in the rhombohedral BiI_3 type [38], or in monoclinic AlCl_3 structure type [39]. In the BiI_3 structure, the honeycomb net is regular due to the three-fold symmetry, with three equal length metal-metal bonds. In the AlCl_3 structure, on the other hand, the honeycomb net can be distorted, and the y -coordinate of the M site determines the degree of distortion. This results in two unique in-plane M - M distances. Most compounds re-

port a temperature driven transition from uniform rhombohedral BiI_3 type to bond-dimerized monoclinic AlCl_3 structure. The available data [35] shows this structural transition typically happens around 100-200 K for d^1 transition metal tri-halides. In the discussion in the following, we will focus on the AAA stacked high temperature structure of uniform honeycomb net of transition metals possessing C_3 symmetry, which would host different possible electronic instabilities. As discussed later, subtle structures in the electron band structure paves the way to electronically driven charge-density-wave instabilities including dimerization, to which the lattice may react.

Although considered structures hold a uniform hexagonal network of metal atoms, the underlying rhombohedral symmetry allows for the trigonal distortion of the MX_6 octahedra, which occurs as the elongation or compression along one of the four three-fold symmetry axis, as shown in Figure 1(b). The elongation (compression) results in decrease (increase) of the angle (θ) between the M-X bond and the three-fold axis from ideal value of 54.73° . Figure 1(b) shows the crystal splitting of the d -levels of M atoms. In presence of the octahedral splitting, the five-fold degenerate d -levels split into three-fold degenerate t_{2g} and two-fold degenerate e_g^σ . In presence of trigonal distortion of the MX_6 octahedra, the t_{2g} levels further split into singly degenerate a_{1g} and doubly degenerate e_g^π , with Δ_2 and Δ_1 denoting the octahedral

and trigonal splitting, respectively.

As mentioned above, in the present study, we focus on the nine d^1 MX_3 compounds with $M=Ti, Zr, Hf$ and $X=F, Cl, Br$, drawn from 3d, 4d and 5d transition metal series and 2p, 3p and 4p series, as shown in Fig. 1(d). The choice of these compounds, allows one to study the interplay of SOC and hopping, as well as Coulomb interaction. Moving down the column, the SOC increases due to increase in atomic number, as well as the metal-metal hopping increases due to increase in the spatial extent of the d -orbitals. Out of the nine proposed compounds, only three compounds, namely $TiCl_3$ [35, 36], $TiBr_3$ [40] and $ZrCl_3$ [41] have been experimentally synthesized. To predict the crystal structure of the remaining compounds, we use the available experimental structure of the related compound with either common M or common X as the template and accordingly substitute the metal or the halide atom with the desired element. The constructed structure is subsequently fully relaxed by relaxing the atomic coordinates and the volume, fixing the symmetry. The influence of exchange-correlation and van der Waals interaction were checked in terms calculations within GGA, GGA+U and GGA+U+D2. Among these, GGA calculation consistently was found to reproduce well the experimentally measured in-plane lattice constants for compounds that have been synthesized. Since we are primarily interested in in-plane physics, in subsequent analysis we consider GGA optimized crystal structures in $P\bar{3}1m$ space group. The optimized values of in-plane lattice parameters as well as trigonal distortion ($\Delta\theta_{trig}$) are given in Table I. The in-plane lattice shows an expansion in moving from 2p to 3p to 4p, and from 3d to 4d to 5d. Interestingly, we note the trigonal distortion in fluoride compounds is opposite to that in chloride and bromide.

IV. DFT BAND STRUCTURE

The GGA density of states of the representative compound $ZrCl_3$, over a broad energy scale of - 7 eV below Fermi level (E_F) and 4 eV above E_F , projected onto Zr d and Cl p states is shown in Fig. 2(a). We find a large separation between the predominantly X p -states (beyond ~ 3.5 eV below E_F) and predominantly M d states (around E_F and above), as expected for early transition metal halides. The corresponding band structure, plotted along the high symmetry points of the hexagonal Brillouin zone (BZ) (cf. inset), is shown in Fig. 2(b). As evident from the plot, there are ten spin degenerate bands arising from the d -orbitals of the two M ions in the unit cell that clusters into three groups of 3, 3 and 4 spin degenerate bands. While the highest energy group of four bands belong to e_g^σ symmetry, the lower two groups of three bands (cf. Fig. 2(b,c)), spanning energy range of ~ -0.3 eV to 0.5 eV, and ~ 1 eV to 0.7 eV respectively, are of t_{2g} symmetry. Since the trigonal crystal field splits three t_{2g} 's into 2+1 at each site, this cannot account for

the above splitting of the six t_{2g} bands into 3+3. At any rate, the trigonal splitting arising from a distortion of 1-2° (cf Table. I) is expected to much smaller compared to the splitting between the two groups, which is about 0.5 eV, as seen in the plot. To resolve this issue, we compute the charge densities corresponding to the 3+3 groups of bands which are shown in Fig. 2(c). As is evident from the charge density plots, the grouping of six t_{2g} bands into 3+3 arises due to bonding-antibonding combination of t_{2g} orbitals resulting from highly directional, direct overlap of t_{2g} orbitals along the three M-M bonds. The band structure plots in Fig. 2(c), zoomed onto two t_{2g} manifolds, show also the computed band structure including SOC. As is seen, SOC has a negligible effect on the entire band structure except lifting degeneracy at the high symmetry points, Γ K, and M, which suggest strength of SOC to be relatively weak, and far from the assumption of infinite SOC limit.

The above discussed broad features of the electronic structure are found in other compounds as well, though they differ in details. For a comprehensive analysis of the t_{2g} manifold of band structure of all nine MX_3 compounds, see Fig. 3. Moving along the metal series, we find while Zr and Hf share similar band structure features, that of Ti is different in terms of the individual bandwidths of the bonding and antibonding blocks, as well as in the separation between bonding and antibonding blocks. This translates into weakening of the direct metal-metal hopping and relative strengthening of indirect hopping via halide ion in Ti compounds, compared to Zr or Hf . Moving along the halogen series, fluoride compounds exhibit markedly different dispersion compared to chloride or bromide counterparts, hinting electronic properties of fluorides to be different from chloride/bromide. A bulk of the discussion, therefore, will concentrate on the chlorides and bromides while we summarize briefly the fluorides in Sec. VII.

V. EFFECTIVE LOW ENERGY TIGHT BINDING MODEL

With the above DFT results, we now turn to the low energy modeling of the above band structure via effective low energy tight-binding Hamiltonian for the t_{2g} orbitals in the presence of SOC.

According to the molecular orbital theory [42], any two t_{2g} orbitals on adjacent sites can interact to form six levels as σ^* , π^* , δ^* , σ , π , δ where, we rank them from the highest to the lowest energy. The energy levels σ and σ^* are the consequence of the direct head-on overlap of the d -orbitals lobes called $dd\sigma$, whereas direct lateral overlap of d orbitals known as $dd\pi$ and ddd , gives rise to π^* , δ^* , π , δ levels respectively. Among these, δ bonds are weakest and neglected henceforth. These overlaps, along with indirect overlaps via the halide ion, dictate the nature of the resultant tight-binding model in t_{2g} basis for single electron kinetic energy which is the starting point for our

	TiX ₃			ZrX ₃			HfX ₃		
	F	Cl	Br	F	Cl	Br	F	Cl	Br
a=b(Å)	5.202	6.030	6.405	5.487	6.204	6.524	5.320	6.096	6.423
$\Delta\theta_{trig}$ (in degree)	2.078	-0.550	-0.714	1.568	-1.133	-1.563	0.815	-1.244	-1.563
Exper. synthesis	No	Yes[36]	Yes*[40]	No	Yes†[41]	No	No	No	No

TABLE I: In-plane lattice constants ($a=b$) and trigonal distortion ($\Delta\theta_{trig}$) of the theoretically optimized structures of MX_3 . Given are also the information on experimentally synthesized compounds. *: structure with space group 148 (ABC stacking) is available, †: based on misaligned powder x-ray data.

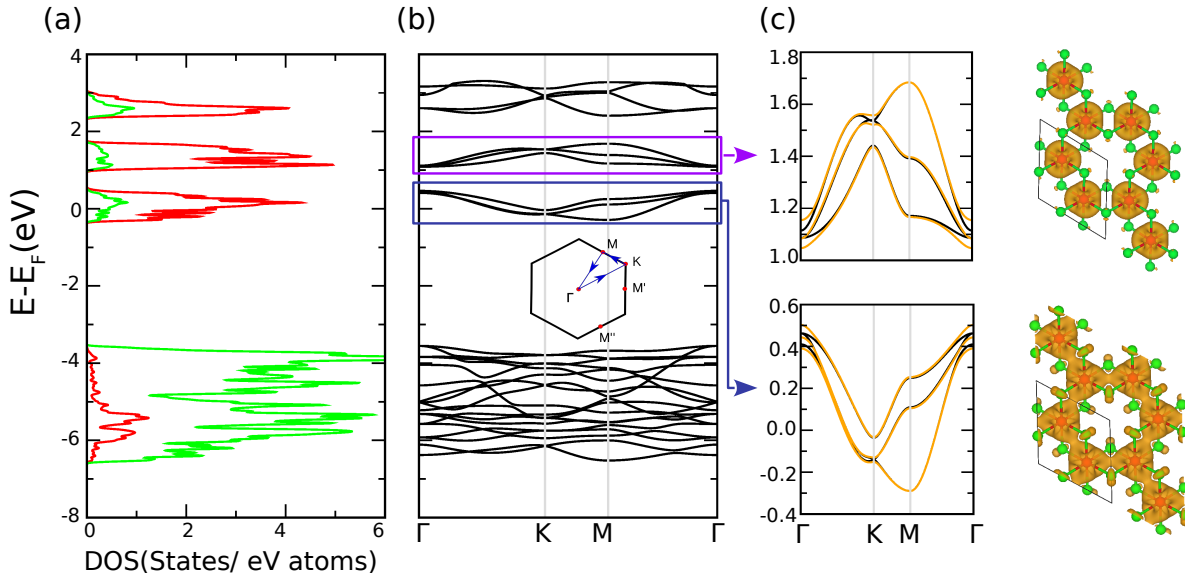


FIG. 2: (a) GGA density of states of $ZrCl_3$, projected to Zr-d (red) and Cl-p (green) states. (b) The corresponding band-structure plotted along the high symmetry points of the hexagonal BZ (shown as inset). (c) Zoomed-in band structure of bonding and antibonding t_{2g} bands and the associated charge densities, with iso-surface value chosen to be $0.009 e^-/\text{\AA}^3$. The zoomed-in band structure plot also includes the comparison of GGA (black) and GGA+SOC (yellow) bands. The zero of the energy in the density of states and band structure plots are set at corresponding Fermi energy.

low energy analysis.

In order to provide the realistic estimates of these direct and indirect overlap mediated hopping integrals, we derived the low-energy Hamiltonian in the effective transition metal t_{2g} Wannier basis, starting from the full DFT band structure. For this purpose, we constructed the effective Wannier functions, by keeping only the metal t_{2g} degrees of freedom in the basis and integrating out the rest through the NMTO-downfolding technique. Fig. 4 (a) shows the comparison of the band structure in the downfolded basis, in comparison to the full band structure. The good comparison, justifies the effectiveness of the prescription followed in deriving the low-energy model.

The real-space representation of the downfolded bands shows non-zero hopping amplitudes up to the 4-th near-

est neighbor (NN) among metal ions. However, a more amenable minimal hopping model with only first NN interaction is sufficient to reproduce most of the qualitative and quantitative features of the bands, as can be seen in Fig. 4 for $ZrCl_3$. Similar conclusion holds also for other materials.

The resultant first NN tight-binding Hamiltonian in t_{2g} basis consists of four essential hopping amplitudes, as given below. For details of transformation between different coordinate systems see SM.[23]

- The direct overlap between neighboring t_{2g} -orbitals that forms a σ -bond denoted by $t_{dd\sigma}$ (cf. Fig. 5(a) left panel, shown for the representative case of $ZrCl_3$).
- The direct overlap between neighboring t_{2g} -orbitals

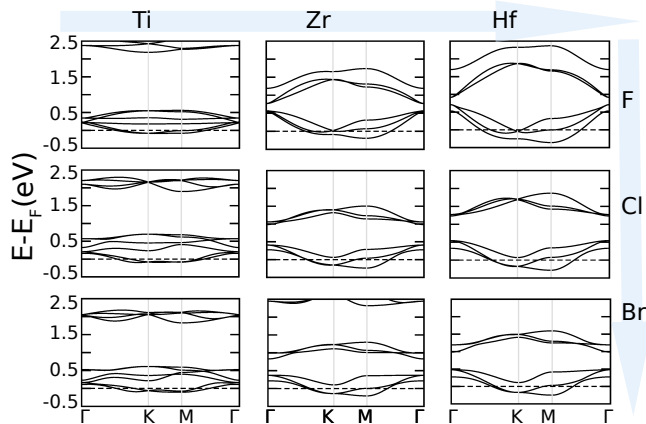


FIG. 3: The variation in band-structure of MX_3 , upon change of metal ion from 3d Ti \rightarrow 4d Zr \rightarrow 5d Hf, along the row, and change of halogen from 2p F \rightarrow 3p Cl \rightarrow 4p Br, calculated within GGA. Fermi energy is set to zero in the plots.

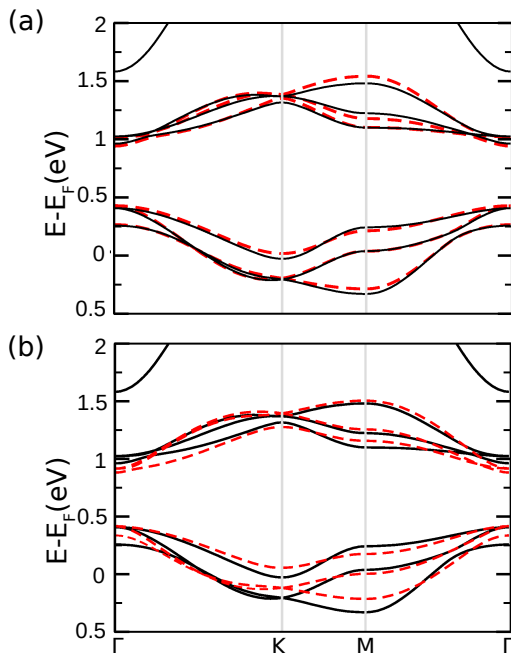


FIG. 4: (a) Downfolded t_{2g} bands (in red) of ZrCl_3 , obtained by integrating all of the degrees of freedom other than Zr t_{2g} in comparison to the DFT band structure (in black). (b) The tight-binding bands (in red), obtained by restricting the real-space representation of the downfolded t_{2g} Hamiltonian to only nearest neighbor Zr-Zr hopping, in comparison to the DFT band structure (in black). Zero of the energy is set at Fermi energy in (a) and (b).

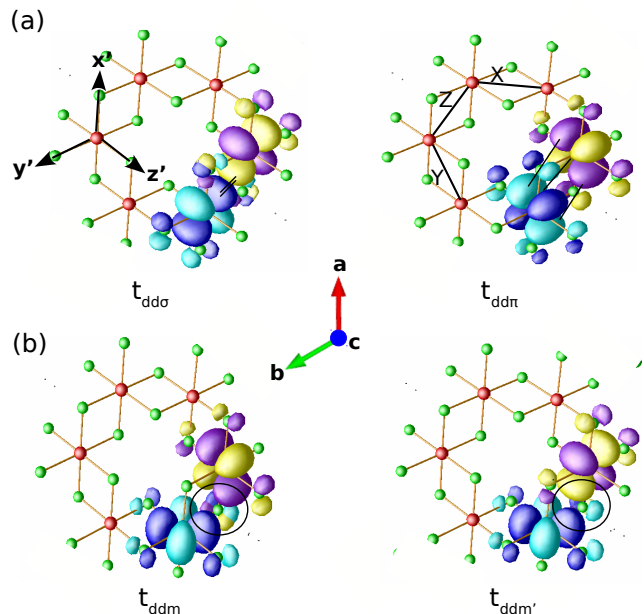


FIG. 5: Overlap of effective t_{2g} Wannier functions in the downfolded basis of ZrCl_3 , placed at two neighboring positions of Zr ions. Lobes of opposite signs are colored as blue (yellow) and cyan (violet) for two different Zr ions. (a) Direct dd overlaps, with left panel showing the head-on overlap ($dd\sigma$) and right panel showing the lateral overlap ($dd\pi$). The overlaps are highlighted by lines. The t_{2g} orbitals are defined with the choice of local primed halogen-based coordinate systems, shown in left panel. The X, Y and Z M-M connecting bonds are shown in the right panel. The crystallographic coordinate system in terms of a, b and c is also shown. (b) Indirect overlaps via the halogen site, between the same (left) and differently shaped (right) t_{2g} functions, labeled as ddm and ddm' in the text. Overlap region via halogen is encircled

that forms a π -bond denoted by denoted by $t_{dd\pi}$ (cf. Fig. 5(a) right panel, shown for ZrCl_3).

- Two indirect overlap between neighboring t_{2g} -orbitals via the halides in the edge-sharing octahedral geometry denoted by t_{ddm} , $t_{ddm'}$, illustrated in Fig.5(b), for ZrCl_3 .

Note that in addition to the above hopping parameters, we also have the on-site trigonal energy scale. However, we find that in presence of dominant effect of $t_{dd\sigma}$ – responsible for creating the bonding and the anti-bonding orbitals (cf. Fig.2(c)), the effect of the trigonal distortion within each manifold of bonding or antibonding bands is minimal and hence we disregard it compared to the other hopping parameters. The results, discussed in the following, is not influenced by this assumption, as has been explicitly checked.

With this, one can now write down the first NN hopping model for the t_{2g} orbitals as

	TiX ₃			ZrX ₃			HfX ₃		
	F	Cl	Br	F	Cl	Br	F	Cl	Br
$t_{dd\sigma}$	-0.167	-0.220	-0.164	-0.546	-0.558	-0.476	-0.708	-0.666	-0.569
$t_{dd\pi}$	0.077	0.062	0.046	0.210	0.150	0.126	0.274	0.190	0.157
t_{ddm}	0.058	0.078	0.079	-0.061	0.030	0.038	-0.126	0.015	0.031
$t_{ddm'}$	-0.022	-0.030	-0.027	-0.023	-0.020	-0.020	-0.039	-0.022	-0.020
$t_{dd\pi}/t_{dd\sigma}$	-0.463	-0.281	-0.277	-0.385	-0.269	-0.264	-0.387	-0.285	-0.277
$t_{ddm}/t_{dd\sigma}$	-0.351	-0.357	-0.481	0.112	-0.053	-0.081	0.178	-0.022	-0.054
$t_{ddm'}/t_{dd\sigma}$	0.134	0.136	0.163	0.043	0.037	0.042	0.055	0.033	0.035
λ	0.015	0.028	0.040	0.030	0.043	0.043	0.060	0.152	0.152
$\lambda/t_{dd\sigma}$	-0.089	-0.127	-0.244	-0.055	-0.076	-0.090	-0.085	-0.228	-0.267
$\Delta = E_{e_g} - E_{A_{1g}}$	-0.030	0.050	0.039	-0.178	0.057	0.077	-0.212	0.065	0.088
$\Delta/t_{dd\sigma}$	0.180	-0.227	-0.236	0.325	-0.103	-0.161	0.300	-0.097	-0.154

TABLE II: DFT estimated hopping terms defined for h_z matrix (cf. Eqn(2)) and SOC strength(λ). The last two rows show energy splitting in t_{2g} level due to trigonal distortion. Apart from ratios, all the numbers quoted are in unit of eV.

$$H_{tb} = \sum_{\langle ij \rangle} \sum_{\alpha, \beta} \sum_{\eta, \eta'} \Psi_{i\alpha\eta}^\dagger \left[h_{ij}^{\alpha\beta} \delta_{\eta\eta'} \right] \Psi_{j\beta\eta'}. \quad (1)$$

Here $\Psi_{j\alpha\eta}$ annihilates electrons at the j 'th site of the lattice with spin η ($=\uparrow, \downarrow$), in the orbital α ($=xy, yz, zx$). The h_{ij} is a 3×3 Hermitian matrix at the bond connecting the i 'th and the j 'th sites of the lattice as shown in Fig. 5(a).

Keeping in mind the different kinds of overlaps of the t_{2g} orbitals, we can write the h_{ij} matrix for the Z -bond as

$$h_Z = \begin{pmatrix} t_{dd\sigma} & t_{ddm'} & t_{ddm'} \\ t_{ddm'} & t_{dd\pi} & t_{ddm} \\ t_{ddm'} & t_{ddm} & t_{dd\pi} \end{pmatrix} \\ = t_{dd\sigma} h_\sigma + t_{dd\pi} h_\pi + t_{ddm} h_m + t_{ddm'} h_{m'} \quad (2)$$

where $t_{dd\sigma}, t_{dd\pi}, t_{ddm}, t_{ddm'}$ are hopping due to direct and indirect overlaps of the orbitals as discussed before. Also, h_σ, h_π, h_m and $h_{m'}$ are 3×3 matrices given by

$$h_\sigma = \begin{pmatrix} 1 & 0 & 0 \\ 0 & 0 & 0 \\ 0 & 0 & 0 \end{pmatrix}, \quad h_\pi = \begin{pmatrix} 0 & 0 & 0 \\ 0 & 1 & 0 \\ 0 & 0 & 1 \end{pmatrix}, \\ h_m = \begin{pmatrix} 0 & 0 & 0 \\ 0 & 0 & 1 \\ 0 & 1 & 0 \end{pmatrix}, \quad h_{m'} = \begin{pmatrix} 0 & 1 & 1 \\ 1 & 0 & 0 \\ 1 & 0 & 0 \end{pmatrix}. \quad (3)$$

The form of the hopping of the X and Y bonds can be obtained by exploiting the three-fold rotation symmetry of the lattice, as detailed in the SM [23].

The DFT estimates for the hopping amplitudes, $t_{dd\sigma}$ etc. for different materials are given in Table II. For different materials, the generic hierarchy of the relative strengths of the hopping parameters are found to be as follows

$$|t_{dd\sigma}| > |t_{dd\pi}| \gg |t_{ddm}| \geq |t_{ddm'}|. \quad (4)$$

The low energy effective tight binding model can be obtained by adding atomic SOC to Eq. 1, which, after appropriate scaling, we write as :

$$\mathcal{H} = \mathcal{E} \sum_{\langle ij \rangle} \sum_{\alpha, \beta} \sum_{\eta, \eta'} \Psi_{i\alpha\eta}^\dagger \left[H_{ij}^{\alpha\beta} \delta_{\eta\eta'} - \tilde{\lambda} \mathbf{l}_{\alpha\beta} \cdot \mathbf{s}_{\eta\eta'} \delta_{ij} \right] \Psi_{j\beta\eta'}. \quad (5)$$

where we have introduced the overall energy-scale

$$\mathcal{E} = |t_{dd\sigma}| + |t_{ddm}|. \quad (6)$$

such that H_{ij} can be obtained by re-scaling h_{ij} (Eq.1) and in particular its form on the Z bond is obtained by re-scaling Eq. 2 as

$$H_Z = -(1 - \tau_m) h_\sigma + \rho \tau_m h_m + r(1 - \tau_m) h_\pi + \tau_m' h_{m'} \quad (7)$$

with

$$t_{dd\sigma} = -\mathcal{E}(1 - \tau_m); \quad t_{dd\pi} = r t_{dd\sigma}; \quad t_{ddm} = \rho \mathcal{E} \tau_m; \\ t_{ddm'} = \mathcal{E} \tau_m'; \quad \lambda = \mathcal{E} \tilde{\lambda}. \quad (8)$$

$\lambda (> 0)$ is the strength of SOC and \mathbf{l} 's represent the three $l = 1$ orbital angular momentum matrices while \mathbf{s} are the Pauli matrices that represent the spin degrees of freedom of the electrons. To estimate the SOC in the studied materials, we calculated the band structure within GGA+SOC. The tight-binding fit of the obtained band structure with DFT-derived hopping integrals together with a tunable λ was used to extract the best fit λ value of a given compound. The estimated λ values are listed in Table II.

The Hamiltonian in Eq. 5 leads to a rich set of possibilities even at the non-interacting level which crucially decides the fate of electron-electron interactions and the low energy phases. While in actual materials all the parameters are present, it is instructive to investigate the above tight binding model in steps by gradually incorporating different parameters starting with τ_m and $\tilde{\lambda}$, as taken in the following sections and subsections.

To this end, we note that the parameter $\rho = \pm 1$ indicates that the indirect hopping amplitude t_{ddm} can be of either sign. In particular we find that (see Table II) ZrF_3 and HfF_3 have $\rho = -1$, making the situation markedly different from that of chlorides/bromides, which was already hinted from the band structure (see Fig. 3). This distinct difference of the fluorides arises from the following characteristic features of F – (1) much smaller ionic radius (147 pm), and (2) much higher electronegativity (3.98); compared to chlorine and bromine with ionic radii (electronegativities) of 175 pm (3.16) and 185 pm (2.96) respectively. Since none of the fluoride compounds have been so far synthesized, for the rest of this paper, we shall be concerned with $\rho = +1$ and shall take up the case for fluorides towards the end in Sec. VII.

VI. SINGLE ELECTRON PHASE DIAGRAM

Our first principle calculations show that the major deviation from the indirect hopping model discussed in Ref. [18, 19] is the direct hopping given by $t_{dd\sigma}$. Hence it is useful to gain further insights into the interplay of the direct hopping, indirect hopping and the SOC. This is obtained by using $r = \tau'_m = 0$ in Eq. 7 such that $\tau_m = 0(1)$ corresponds to the purely direct (indirect) hopping limits at different values of SOC. The importance of direct metal-metal interaction, over the conventional description of ligand-mediated interaction in description of phenomenology of transition metal compounds, has been acknowledged in recent time, in context of cobaltates. [43] The resultant phase diagram forms the basis to understand the material relevant final phase diagram which we obtain by sequentially turning on $t_{dd\pi}$ and t_{ddm} .

A. Phase diagram for $\tau_m - \tilde{\lambda}$ model

The phase diagram in the $\tau_m - \tilde{\lambda}$ plane is shown in Fig. 6(a). The top right corner, $P_3 (\equiv \tau_m = 1, \tilde{\lambda} = \infty)$ corresponds to infinite SOC in the purely indirect hopping limit with infinite coupling. This, for d^1 gives rise to SU(8) Dirac semi-metal (DSM) as discussed in Ref. [19]. At P_3 , the six t_{2g} orbitals (including spin degeneracy) split up into four $J = 3/2$ and two $J = 1/2$ orbitals which are separated by infinite energy gap ($\propto \tilde{\lambda}$) with the $J = 3/2$ orbitals being of lower energy. Hence at this point we obtain 1/4th filled $J = 3/2$ orbitals whose band structure is shown in inset (V) of Fig. 6(a). Here, the lowest band linearly touches the upper band at the Γ and the M points of the BZ giving rise to four 4-component Dirac fermions sitting at four valleys – the three M points of the BZ and one at the Γ point that constitutes the SU(8) DSM [19]. Remarkably, almost the entire phase diagram, except the pink and green shaded parts along the $\tau_m = 0$ and $\tilde{\lambda} = 0$ axis, can be understood from this SU(8) limit as we now discuss.

On moving away from the SU(8) point, all the Dirac fermions get gapped out, generically giving rise to band insulators. However the nature of these two band insulators obtained in the two extreme limits of changing τ_m or $\tilde{\lambda}$ away from P_3 , are different. One of them – that obtained by varying only τ_m – is a free fermion symmetry protected topological phase (SPT) [22], as is evident from the gapless edge modes plotted in Fig. 6(b). These edge modes are protected by time reversal symmetry. Indeed out of the 24 distinct ways of gapping out the SU(8) Dirac fermions discussed in Ref. [19], there are precisely two different time reversal invariant lattice (\mathcal{A}_{1g}^e) singlet masses where we have used the notations of Ref. [19] for ready reference. The above two band insulators correspond to these two singlets as detailed in SM [23]. The two insulating phases are separated by a phase transition denoted by the magenta curve connecting the points P_3 and $P_1 \equiv (\tau_m = 0.67, \tilde{\lambda} = 0)$. On this line, only the Dirac fermions at the Γ point becomes gapless while those at the three M-points remain gapped across the transition as shown in the band-structure (VI) in Fig. 6(a). The resultant theory has an enhanced SU(2) symmetry as detailed in SM [23].

In Fig. 6(a), diametrically opposite to P_3 is the point $O \equiv (\tau_m = 0, \tilde{\lambda} = 0)$ which describes the purely direct hopping model via $t_{dd\sigma}$ without SOC. Here, the Hopping Hamiltonian (Eq. 5) reduces to a particularly simple form, given by

$$H = -\mathcal{E} \left(\sum_{\langle ij \rangle \in Z\text{-bonds}} \Psi_{i,xy,\eta}^\dagger \Psi_{j,xy,\eta} + \sum_{\langle ij \rangle \in X\text{-bonds}} \Psi_{i,yz,\eta}^\dagger \Psi_{j,yz,\eta} + \sum_{\langle ij \rangle \in Y\text{-bonds}} \Psi_{i,zx,\eta}^\dagger \Psi_{j,zx,\eta} \right) + h.c. \quad (9)$$

such that on the Z/X/Y-bonds (See Fig. 5(a)) respectively only the $xy/yz/zx$ -orbitals hop. Since each set of bonds forms a disconnected network of dimers that rotate into itself under C_3 , we get bonding and anti-bonding orbitals of the respective types on each of the three bonds resulting in two sets of 6-fold (including spin $\eta = \uparrow, \downarrow$) degenerate flat band as shown in inset (III) of Fig. 6(a). This is evident in the form of the Wannier functions obtained from DFT (cf. Fig. 5). This kind of separation of the energy bands into two groups of three bands is also seen in the DFT band structures of ZrCl_3 shown in Fig. 2(c), which is dominated by the direct overlap $t_{dd\sigma}$ as given in Table II.

The fact that the entire OP_1 segment on the $\tilde{\lambda} = 0$ line is gapless is expected on very general grounds and is in fact dictated by the general structure of the phase diagram starting from the SU(8) symmetric point, P_3 . This can be rationalized based on that fact on this line there is an enhanced SU(2) spin rotation symmetry such that this line cannot be a part of the free fermion SPT

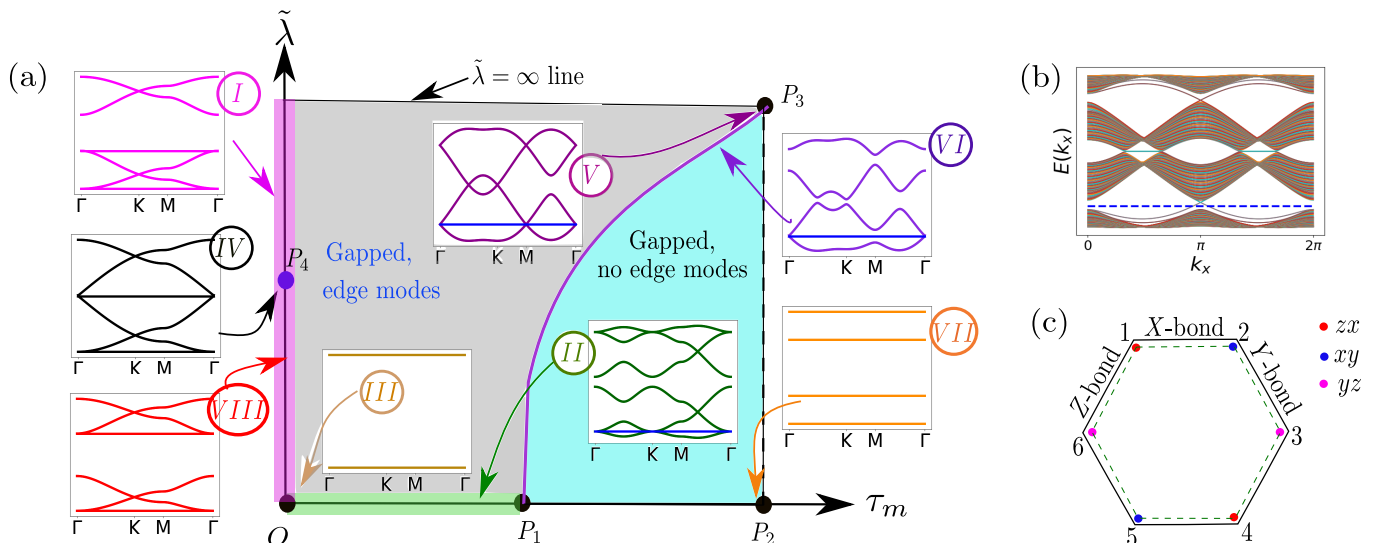


FIG. 6: (a) Phase diagram in $\tau_m - \tilde{\lambda}$ plane for $r = 0, \tau'_m = 0, \rho = +1$. The two gapped phases are shown with different colors (gray and cyan). The band structures, plotted along the Γ , K and the M points of the BZ. at different points on the phase diagram are shown as insets. The blue horizontal lines in the insets II, V and VI show the position of the Fermi level. In the inset II, both the bands are six-fold degenerate as explained in the text. The insets V and VI are for very large value of $\tilde{\lambda}$ and hence the only the four lower energy $J = 3/2$ bands are shown. (b) Band structure in the topological gapped phase (for $\tau_m = 0.9, \tilde{\lambda} = \infty, r = 0, \tau'_m = 0$) in cylindrical geometry. The edge modes at the Fermi-energy are shown by the blue solid line, with Fermi level marked in dashed line. (c) A single hexagon showing the origin of molecular orbitals at point P_2 of the phase diagram in Fig 6(a). Different colored dots represent three t_{2g} orbitals. The six sites of the hexagon are labeled with numbers from 1 to 6. The symmetric linear combination of the orbitals connected by the green dotted line form the lowest energy band. Other orbitals are localized on singles bonds of the hexagon are shown by black dotted lines. See text for details.

lying above it for finite $\tilde{\lambda}$ – as predicted by the SU(8) theory. The trivial insulating phase (shown in cyan in Fig. 6(a)) of course can be connected to the spin-rotation symmetric segment $P_1 P_2$ continuously. Finally at the point $P_2 \equiv (\tau_m = 1, \tilde{\lambda} = 0)$, the bands become flat again with a degeneracy of 2-4-4-2 (inset (VII) of Fig. 6(a)). At this point (P_2), the lowest band is made up of spin-degenerate *molecular orbitals* of the type shown in Fig. 6(c) at each hexagon. On deviating from this point, these orbitals acquire dispersion. Hence the entire gapped trivial insulator (shown in cyan in Fig. 6(a)) can be understood in terms of these effective eigenmodes.

On increasing the SOC ($\tilde{\lambda}$) along the $\tau_m = 0$ line in Fig. 6(a), the six-fold symmetry is independently lifted in the bonding and anti-bonding sectors without intermixing for small $\tilde{\lambda}$ as shown in inset (VIII) of the figure. The band structure (inset (VIII)) is very similar to that of monolayer Kagome band structure [44] – for both the bonding and anti-bonding sectors – with the lower dispersing band touching the flat band quadratically at the Γ -point of the BZ. As one increases the SOC, the band-width of each of the two sectors increases while retaining their overall shape such that at the point $P_4 \equiv (\tau_m = 0, \tilde{\lambda} = 1.35)$ the bands touch at the Γ point leading to a spin-1 Dirac dispersion [45] at the touching of the two sectors (inset (IV) of Fig. 6(a)). On increasing SOC further, remarkably the second flat band – previously associated

with the anti-bonding sector – detaches from it and becomes a part of the bonding sector leading to a division of four lower bands (inset (I) of Fig. 6(a)) – as expected from the $J = 1/2$ and $J = 3/2$ splitting of the atomic orbitals at large SOC. For d^1 materials, however, the above change of band structure is not important as only the lowest flat band is filled such that the chemical potential lie at the lowest quadratic band touching points leading to a very unstable (to interactions) quadratic band-touching semimetal with one of the flat bands having divergent effective mass.

The above structure of the phase diagram gives a good starting point to connect to the DFT band structure by incorporating the sub-leading interactions as we now turn to discuss. Two such important sub-leading parameters are $t_{dd\pi}$ and $t_{ddm'}$ representing the sub-leading direct and indirect hopping respectively (see Eqs. 2 and 8 as well as Table. II). We study their effects as a build up to the material phase diagram.

1. Effect of $t_{dd\pi}$

The first sub-leading hopping that is relevant across all the compounds is the direct hopping via the π -overlap denoted by $t_{dd\pi}$ as shown in Fig. 5 and incorporated via the

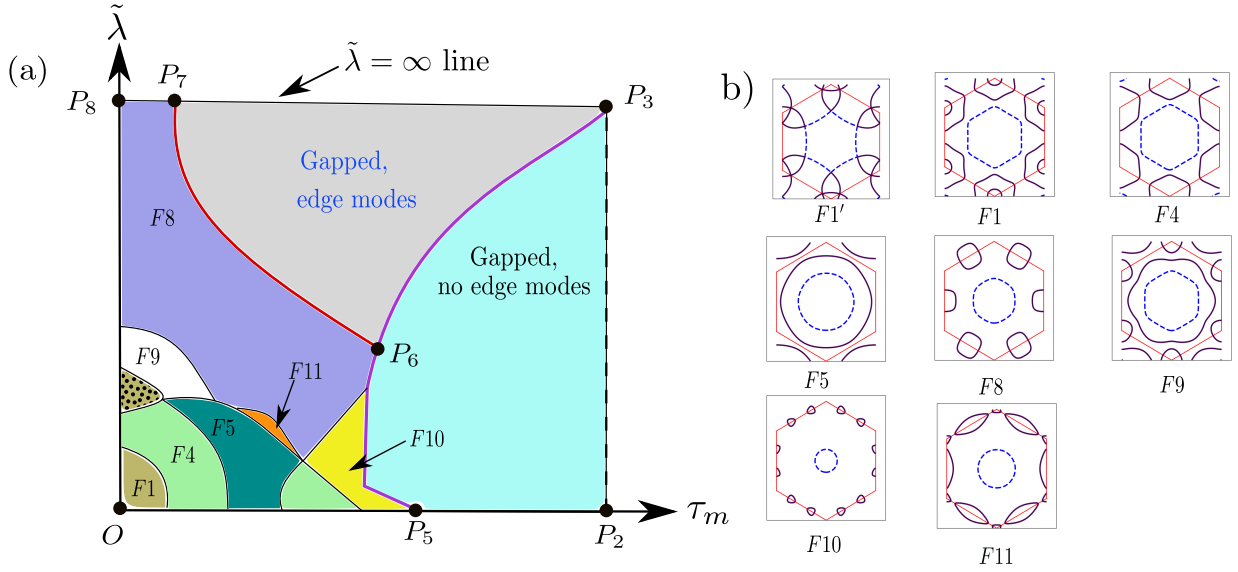


FIG. 7: (a) Phase diagram for $\rho = +1, r = 0.3, \tau'_m = 0$. Two gapped phases shown in gray and cyan shading. The different metallic phases are shown with different colors and labeled as $F1, \dots, F11$. (b) Fermi surfaces corresponding to different metallic phases. The hole-like Fermi surfaces are shown with blue dashed lines and the electron-like FS are shown with solid violet lines. The hexagonal BZ is shown with red solid lines. The $F1'$ Fermi surface corresponds to the O point of the phase diagram shown in panel (a). The un-dotted and dotted region of $F1$ differ by the factor for the Fermi surface corresponding to the dotted region, one of the Fermi pockets around the K points is electron-like and the other is hole-like, while both are electron-like for the un-dotted region.

parameter $r = |t_{dd\pi}|/|t_{dd\sigma}|$ in our effective tight-binding Hamiltonian (Eq. 5) as shown in Eq. 8. However, instead of scanning the entire phase diagram as a function of r , we shall confine ourselves to $r = 0.3$ —a value which is roughly consistent for the different materials. The resultant phase diagram is shown in Fig. 7.

The P_2P_3 line of Fig. 7(a) is exactly equivalent to that of Fig. 6(a) and hence the description of the entire trivial gapped band insulator in cyan region remains same apart from the quantitative renormalization of the band structure away from the $\tau_m = 1$ line. Similarly the physics of the $\tilde{\lambda} = \infty$ for $\tau_m < 1$ holds until the point P_7 giving rise to the Z_2 free fermion SPT (gray region) with gapless edge modes, exactly in the case of $t_{dd\pi} = 0$ in Fig. 6(a). The intermediate line, P_3P_6 , hence is associated with a Dirac band-touching at the Γ -point of the BZ giving rise to a $SU(2)$ DSM. However, the effect of $t_{dd\pi} = r|t_{dd\sigma}| \propto (1 - \tau_m)$ drastically rearranges the band structure for lower τ_m , as we discuss now.

The $t_{dd\pi}$ lifts the threefold degeneracy of the flat bands at the point $O = (\tau_m = 0, \tilde{\lambda} = 0)$ leading to dispersive bands that cross the chemical potential giving rise to a compensated band metal such that the net Luttinger volume is zero. The relevant Fermi surface is named $F1'$ and is shown in Fig. 7(b). However this is highly unstable due to the touching of the hole and particle Fermi pockets and on increasing both τ_m and $\tilde{\lambda}$, the resultant Fermi surface undergoes topological changes giving rise to a plethora of compensated band metals denoted by $F1 - F11$ in Fig. 7(a). The intervening Lifshitz transi-

tions [46, 47] include cases where both separate sheets of Fermi surfaces merge, e.g. $F4$ to $F5$ via van-Hove singular necks, as well as, instances where individual sheets of Fermi surfaces disappear, e.g. $F1$ to $F4$. This generic appearance of the compensated band metals with diverse Fermi-surface topology is particularly relevant to the materials under consideration as we discuss in the next section in detail along with the relevant Lifshitz transitions.

We would like to end this discussion about the effect of $t_{dd\pi}$ by commenting on the metals $F1 - F11$ (Fig. 7(a)) that occupy the region that was erstwhile (Fig. 6(a)) a part of the topological insulator. Interestingly for $F8$, the electron bands evolve continuously from the free fermion SPT and hence it inherits a non-trivial Z_2 invariant for the bands crossing the chemical potential. In fact, except on the $\tilde{\lambda} = 0$ line, we find that for all the metals in the phase diagram under consideration, one of the bands crossing the chemical potential has non-trivial Z_2 index, calculated following the method discussed in Ref. [48]. The method is applicable for systems with inversion symmetry, as is in the present case.

2. Effect of $t_{ddm'}$

We now turn to the effect of the indirect hopping mediated by $t_{ddm'}$ on the minimal model with phase diagram in Fig. 6(a). Again we choose a representative value of $t_{ddm'} = -t_{ddm}$ in the regime relevant to the materials — to indicate its effect. Unlike $t_{dd\pi}$, this indirect hop-

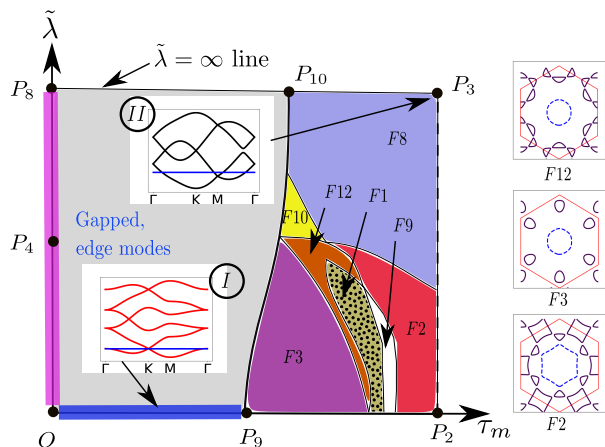


FIG. 8: Phase diagram for $r = 0, \tau'_m = -\tau_m, \rho = +1$. Inset *I* shows a prototypical band structure for a point on the OP_9 line where the lowest band touches the next band linearly at the K points, while the inset *II* shows the band structure at the P_3 point. Since $\tilde{\lambda} = \infty$ at P_3 , only four bands ($J = 3/2$ bands) are shown in inset *II*. As in Fig. 7(a), metallic phases with different Fermi surface topology, are labeled and colored. In addition to $F8, F9$ and $F10$, introduced in Fig. 7(a), three new phases, labeled as $F2, F3$ and $F12$ appear. The Fermi surface topology for $F2, F3$ and $F12$ phases are shown by the side.

ping now drastically reorganizes the $\tau_m \approx 1$ region of the phase diagram—apparent by contrasting Fig. 6(a) with Figs. 7(a) and 8.

In particular the line $\tau_m = 0$ remains unaltered with respect to the minimal model (Fig. 6). Also the free fermion SPT (in gray in Fig. 8) is stable to finite $t_{ddm'}$, albeit it does not extend all the way to the point P_3 . In fact the $SU(8)$ Dirac point (P_3) now develops into a compensated band metal as the Dirac cones, at the erstwhile P_3 point, moves away from the chemical potential in opposite direction—the Dirac node at the Γ point moves above it and those at the M points move below it—giving rise to Fermi pockets around these points. The band structure at the P_3 point is shown in inset *II* of the phase diagram in Fig. 8. The resultant Fermi surface around this point is of $F8$ type given in Fig. 7(b).

As we move away from the P_3 point along the $\tilde{\lambda} = \infty$ line by decreasing τ_m (thus increasing $t_{dd\sigma}$), the $F8$ Fermi surface continues to exist, although a finite gap at the M and the Γ opens up (away from the chemical potential) between the lowest and the second lowest band. This gap opening due to the effect of $t_{dd\sigma}$ gives a non-trivial Z_2 number to the lowest band and hence the $F8$ metal in the phase diagram in Fig. 8 is a topological metal. On moving further away from the P_3 point along the $\tilde{\lambda} = \infty$ line, the size of the Fermi pockets of the $F8$ metal continuously shrink and eventually vanish at the P_{10} point after which the system enters into a gapped phase. Since this transition from the $F8$ metal to the

gapped phase does not happen through a band touching, the Z_2 invariant of the lower band remains unchanged across this transition and hence the gapped phase is also topological insulator—the same free fermion SPT as in Fig. 6.

Turning to low SOC, the P_2 point no longer has flat bands but now gains a dispersion due to τ'_m leading to a compensated metal of Fermi surface type $F2$ as shown in Fig. 8. On moving from the point away from the P_2 point along the $\tau_m = 1$ line, the $F2$ Fermi surface transforms into a $F8$ type Fermi surface, which is then connected to the P_3 point. This $F8 - F2$ transition does not involve any band touching, but just a change of the chemical potential and hence the $F2$ region of the phase diagram is also a topological metal. On reducing the values of τ_m from the point P_2 , the system encounters various other metallic phases which have different Fermi surfaces ($F9, F1, F12, F3$ etc.). We find that for all these phases, the bands crossing the Fermi energy always have a nontrivial Z_2 index. Thus, all the metals in this phase diagram are also topological metals.

Finally, on the line OP_8 , $\tau_m = \tau'_m = 0$ and hence the description of this line is the same as in the phase diagram in Fig. 6. On the other hand, along the OP_9 line (for which $\tilde{\lambda} = 0$), the lowest band touches the upper band linearly at the K points. The effect of finite $\tilde{\lambda}$ opens up gap at the K points and the system enters into the topological gapped (gray shaded region).

B. The material phase diagram

Having discussed the minimal tight-binding model and the effect of the sub-leading hopping terms resulting in a rich single-particle phase diagram, we now turn to the regime that may be most suited to the material parameters, except for the fluorides. To this end we choose the representative hyperplane given by $\rho = +1, r = 0.3, \tau'_m = -\tau_m$ and vary $\tau_m \in (0, 1)$ and $\tilde{\lambda} \in (0, \infty)$.

The phase diagram in this parameter regime is shown in Fig. 9. Due to the complementary effects of the secondary direct and indirect hopping— $t_{dd\pi}$ and $t_{ddm'}$ respectively—the resultant phase diagram is in a way superposition of Figs. 8 and 7(a) such that all the phases appearing in this case are gapless, perfectly compensated and have Fermi surfaces with at least one partially filled band having non-trivial Z_2 invariant.

Based on which particular band(s) carry non-trivial Z_2 , the phase diagram can be demarcated by red, magenta and blue lines (see Fig. 9). The Z_2 index for the lowest band is non-zero for the region of the phase diagram which is in the right hand side of the red solid line. On the other hand, the second lowest band has nontrivial Z_2 index for the regions of the phase diagram which are either left to the red solid line or right to the magenta solid line. On the red line, the lowest and the second lowest bands touch at the M point and the Z_2 character of the two bands switch. On the magenta line, the sec-

ond lowest band touches the third lowest band and thus encounters another change in Z_2 character. The third lowest band, which crosses the Fermi energy only at the $F1$ region which is near the origin O , has non-trivial Z_2 index for the region which is left to the blue solid line in the phase diagram. On this blue line, the third lowest band touches the fourth lowest band and encounters a change in Z_2 character.

The positioning of the materials ZrX_3 , TiX_3 and the HfX_3 ($X = Cl, Br$) in the phase diagram, based on the estimated parameters given in Table II is shown in zoomed plots given in Fig. 9. Due to weaker SOC compared to the strength of leading hopping interactions, the studied compounds are all placed towards the bottom of the phase diagram. Given the fact, that $t_{dd\sigma}$ (t_{ddm}) is significantly larger(smaller) in Zr/Hf compounds compared to Ti compounds, as expected, Zr and Hf compounds are placed left to Ti compounds. Given the similarity in electronic structure of Zr and Hf compounds (see Fig. 3), it is not surprising that they belong to the same $F4$ class, with Hf compounds lying higher in position compared to Zr, due to stronger SOC. On the other hand, Ti compounds belong to distinctly different $F5$ class. Systematically, bromine compounds lie higher and right to chlorine compounds, due to stronger SOC and weaker direct hopping strength, respectively.

The detailed Fermi surface(FS)s of the compensated, topological metallic phases of the six compounds are shown in Fig. 10. The $F4$ type FS of ZrX_3 and HfX_3 compounds, is characterized by three disjoint Fermi pockets—two electron-like pocket around the two K points and one hole-like pocket around the Γ point. On the other hand, the TiX_3 compounds having $F5$ -type FS, have two Fermi pockets, one electron-like and one hole-like around the Γ point.

C. Nesting and Lifshitz transitions

A characteristic feature of some of the FSs in Fig. 10 are the flattish *almost nested* sections – involving both intra and inter-pockets. This makes them particularly susceptible to nesting instabilities in presence of electron-electron interactions at appropriate wave-vectors. Our preliminary results indeed indicate enhanced susceptibilities in the charge-density-wave channel due to such nesting. The detailed characterization of such instabilities though require more accurate study particularly due to the intricate structure of the FS's involved.

Another feature of the phase diagram is the presence of plethora of Lifshitz phase transitions [46, 47] between the variety of compensated metals (Fig. 9). These phase transitions involving a change in the Fermi surface topology can be classified into two broad categories [46, 49] – (1) *pocket vanishing* type associated with disappearance of new segments of Fermi surface *e.g.*, between $F1$ and $F4$ where the Fermi pockets centered around the BZ corners appear— possibly relevant for $Zr(Hf)Cl_3$ and

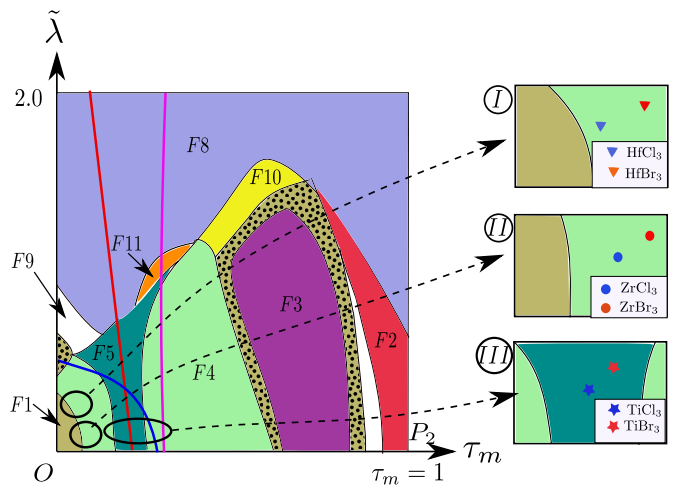


FIG. 9: Phase diagram for $\rho = +1, r = 0.3, \tau'_m = -\tau_m$ with $0 \leq \tau_m \leq 1$ and $0 \leq \tilde{\lambda} \leq 2.0$. For $\tilde{\lambda} > 2.0$, the $F8$ phase continues to exist. The six different chloride/bromide compounds are placed in this phase diagram, according to the estimated parameter values of the low energy Hamiltonian (cf. Table II), shown in the insets I, II and III. The phase diagram is demarcated by the red, blue and magenta lines, according to the Z_2 characters of the bands. See text for details.

$Zr(Hf)Br_3$, and, (2) *neck collapsing* type associated with merging of two segments of Fermi surfaces *e.g.*, the transition between $F4$ and $F5$ where two particle-like Fermi pockets develop a neck that meets at the M points possibly relevant for $TiCl_3$ and $TiBr_3$. These transitions, accessed, in the present case, by tuning the band parameters at a particular filling, occur due to the change of the band-structure at the chemical potential. While the former leads to a step function in the single-particle density of states, $\rho(\epsilon - \epsilon_F) \sim \theta(\epsilon - \epsilon_F)$, the latter has a logarithmic singularity, *i.e.*, $\rho(\epsilon - \epsilon_F) \sim -\ln|\epsilon - \epsilon_F|$ and hence has a van Hove singularity arising from the vanishing Fermi velocity for the electrons on the Fermi surface. This singular behavior can be reflected in thermodynamic measurements such as magnetic susceptibility [49] as well as scaling of bipartite entanglement entropy [50]. Interestingly, the tuning of the band parameters can be achieved through bi-axial straining which should be achievable considering the layered structure of the materials similar to $SrRuO_4$ [51]. Considering about 2% compressive strain on $ZrCl_3$, the direct $dd\sigma$ hopping is found to enhance by about 20% while the indirect hopping is found to be heavily suppressed, thereby conducive to triggering a $F4 \rightarrow F1$ transition. This may be even easier for Hf compounds, which are even closer to the $F4$ - $F1$ boundary. Our DFT calculated FS for 1% strained Hf compound, indeed shows a $F1$ type. Straining on Ti compounds shows similar effect, although the percentage change is found to be much smaller. Therefore such straining may be of interest in investigating the physics of the Lifshitz transition.

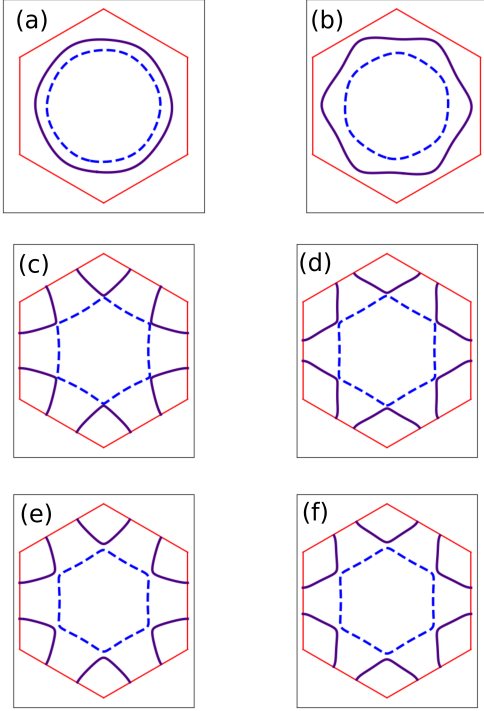


FIG. 10: Fermi surfaces for (a) TiCl_3 , (b) TiBr_3 , (c) ZrCl_3 , (d) ZrBr_3 , (e) HfCl_3 , (f) HfBr_3 . The (a) and (b) are $F5$ -type Fermi surface while the rest are $F4$ type. The blue dotted lines show hole-like Fermi surface and the solid indigo colored lines show electron-like Fermi surface. The red line shows the boundary of the hexagonal BZ.

VII. $\rho = -1$: IMPLICATION FOR FLUORIDES

Having discussed the situation with the chlorides and the bromides, we now turn to fluorides, which as indicated above (cf Table II) show markedly different electronic structure. Furthermore, unlike, chlorides and bromides, the tight-binding parameters for fluorides show diverse behavior even among the 3d, 4d and 5d transition metals, the parameters for Ti being rather different from that of Zr/Hf. This hinders providing a universal framework to describe the three fluoride compounds, captured through a common phase diagram, as was possible for chlorides and bromides. We thus concentrate on the most striking difference between Zr/Hf chlorides and bromides, and Zr/Hf fluorides, namely the change in sign of the indirect hopping, t_{ddm} , captured by the parameter ρ in Eq. 8. This affects some of the basic conclusions stemming from the structure of the minimal phase diagram, presented in Fig. 6. In the following, we thus confine ourselves to the $\tau_m - \tilde{\lambda}$ phase diagram, which determines the nature of the low energy single-particle starting point for these materials, without delving into the complexity of the sub-leading hopping like $t_{dd\pi}$ and

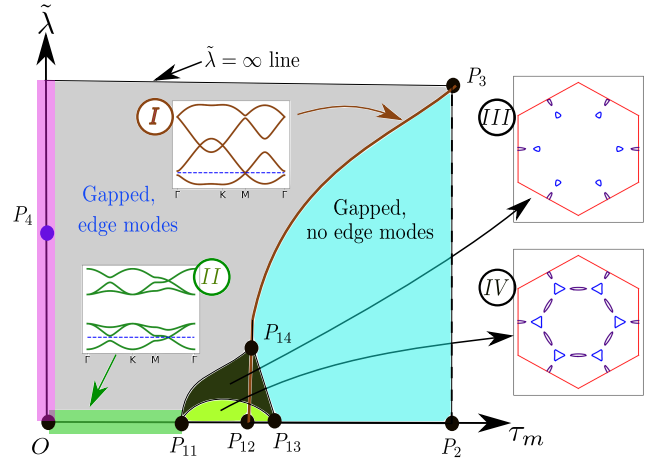


FIG. 11: $\tau_m - \tilde{\lambda}$ phase diagram with $\rho = -1$, $r = 0$, $\tau'_m = 0$. The two gapped phases, shaded as gray and cyan, as well as pink coloured lines in the phase diagram are identical to those in Fig 6(a). The band structures on a typical point on the OP_{11} line is shown in inset II. The inset I shows the band structure on the transition line between the two gapped phases. Note that inset I shows only four bands since it is drawn for a large value of $\tilde{\lambda}$ where the four lower energy $J = 3/2$ orbitals are separated from the higher energy $J = 1/2$ orbitals by a large energy separation. As opposed to Fig 6(a), this phase diagram hosts two topological metallic phases, marked in lime-green and dark green shades. The Fermi surfaces for the two metallic regions are shown by insets III and IV.

t_{ddm} . The obtained results are shown in Fig. 11, which should be contrasted with Fig. 6(a).

First of all, we notice a similarity of the phase diagrams in Fig. 11 and Fig. 6(a), especially for large $\tilde{\lambda}$. This apparent similarity, however hides an important contrast, that can be best understood as follows. Starting from the $SU(8)$ limit, P_3 in the present case, is a *particle-hole* inverted version of Fig. 6(a) due to the change in sign of t_{ddm} . Thus, while the P_3 still gives a $SU(8)$ DSM with four 4-component Dirac points at Γ and three M points, the associated spinors are not necessarily the same as in the previous case, but are related to it via a microscopic particle-hole transformation. In fact this theory is therefore a particle-hole conjugate version of the $SU(8)$ metal discussed in Ref. [19] and hence the same mass analysis can be applied to the present case. It is for this reason, we still have the same two gapped phases– the free fermion topological and trivial band insulators on deviating away from the $SU(8)$ semi-metal– resulting from the two lattice singlet masses [19]. However, the difference in the eigen modes due to the change in sign becomes apparent at the transition between the two insulators, which now is brought about by closing of the gap at the three M points on the line P_3P_{14} while that at the Γ point remains gapped– unlike in case for P_3P_1 line in Fig. 6(a).

This leads to an enlarged SU(6) internal symmetry for the $N_F = 3$ free Dirac fermions on the P_3P_{14} line (see SM).

Another consequence of the above change in the nature of the spinors is the appearance of additional compensated semi metals for lower values of $\tilde{\lambda}$ around $t_{dd\sigma} \sim t_{ddm}$. The corresponding Fermi surfaces are shown in insets III and IV. The lowest bands of these metals have non-zero Z_2 index on the closed region $P_{11}P_{12}P_{14}$, while the upper band is Z_2 -trivial. On the line $P_{12}P_{14}$, the lowest band touches the upper band at the M points and the Z_2 indices of these two bands switch. Thus, one of the bands of these metals always has non-zero Z_2 index and these are topological metals. On the $P_{13}P_{14}$ line, Fermi pockets of the metals shrink to zero and the system enters the trivial insulating phase. Hence, the change of sign of the indirect hopping, makes the situation more favorable to the topological metallic phase, which may be stabilized even without inclusion of sub-leading hopping terms.

VIII. SUMMARY AND OUTLOOK

In summary, following the stimulating proposal of achieving SU(8) DSM state in quarter-filled J=3/2 SOC coupled electrons, we critically examine the material realization of this proposal considering d¹ transition metal tri-halide family of compounds, MX₃. Systematic variation of both the metal site from 3d to 5d (M= Ti, Zr, Hf) as well as the halide site from 2p to 4p (X=F, Cl, Br) allows to study the interplay of different microscopic energy scales. Although only three out of the studied nine compounds have been synthesized so far, we do hope our study will encourage synthesis of other compounds too.

Our first-principle electronic structure calculations in combination with minimal tight-binding models show that a hierarchy of electron hopping pathways is needed to faithfully capture the rich low energy single electron physics in these compounds. Importantly, our study uncovers the dominant role of direct metal-metal hopping. Thus, a minimum of five band parameters – atomic SOC (λ), two direct metal-metal hopping ($t_{dd\sigma}, t_{dd\pi}$), two indirect metal-halide-metal hopping (t_{ddm}, t_{ddm}')– dictate the low energy fermiology. Our study further unravels while the chlorides and bromides have a generic trend of band parameters, the fluorides are distinct – due to the drastic difference in the size and electronegativity of the fluoride ion compared to chloride and bromide.

Inclusion of this material specific reality renders the physics of the above candidate compounds in a domain far removed from the idealized SU(8) DSM. Instead, a variety of topologically non-trivial compensated metals gets stabilized upon variation of relative strength of direct vs indirect hopping and SOC, which differ in their Fermi surface topology. Fermi surfaces with different topology are found to be connected through intervening Lifshitz phase transitions. Remarkably, though, the ideal SU(8) point serves as a useful starting point to understand the

global structure of the above phase diagram. In particular, the compensated metallic phases are found to be asymptotically connected to topological insulating states resulting from gapping out of SU(8) semi-metals. Placing of the compounds, in the emergent in the $t_{dd\sigma}/t_{ddm}$ - λ phase diagram reveals the chloride compounds are close to the phase boundary separating two metals with different Fermi surface topology. Introduction of bi-axial strain in these layered compounds, is found to cause a large variation in the $t_{dd\sigma}/t_{ddm}$, thereby could be an effective tool to induce Lifshitz transition in chloride compounds, in particular.

While the above study captures the physics of non-interacting electrons in the un-dimerized lattice, several possible ordering instabilities can be triggered in these compensated metallic phases at lower temperatures, as discussed in the following. For instance, electron-electron interaction driven ordering instabilities are expected to be particularly enhanced near the Lifshitz transitions [49, 52, 53] due to the singular nature of single-particle density of states. Akin to the neck collapsing Lifshitz transition and associated singular nature of the density of states found in present case, similar phenomena have been discussed in Sr₂RuO₄, which reports enhancement of instability near Lifshitz point[51]. The renormalization group calculations for the short-ranged four fermion interactions near the neck collapsing between two particle-like Fermi pockets indicate an enhancement of the BCS superconducting instability [54, 55]. In particular, the neck collapsing transition at BZ boundary at M points between $F4$ and $F5$ opens up the possibility of finite momentum instabilities in both the particle-hole and particle-particle channels. The former can lead to a charge-density wave insulator generically accompanied by dimerization as observed in some of the candidate materials [35, 56]. The finite momentum pairing instability leading to a (Fulde-Ferrel-Larkin-Ovchinnikov) FFLO-like [57, 58] phases are equally interesting. These issues call for further detailed investigation.

Furthermore, the effect of short-ranged Hubbard interaction, U , supplemented with a Hund's scale, J , relevant for multi-orbital systems energetically favors, within our GGA+U+SOC calculations (see SM for details), a ferromagnetic metal in all the materials for lower values of $U - J$, which in turns gives way to ferromagnetic insulator and/or stripy and zig-zag spin density wave insulators for larger $U - J$ values. This hints towards a profusion of competing interaction effects likely to be in play in the current family of materials, driving the electrons to various ordered states at lower temperatures. We further note the metallic state with net moment and topological character should lead to intrinsic anomalous Hall conductivity.

Finally, while the present study focuses on d¹ honeycomb compounds, it is straightforward to extend these ideas to materials with d³ configuration such as MoCl₃. Our minimal tight-binding model suggests a similarly rich fermiology in such materials including a curious ex-

change of flat band along $\tau_m = 0$ line in Fig. 6. This will be taken up in future.

ACKNOWLEDGMENTS

The authors acknowledge discussion with Arun Paramakanti, H. R. Krishnamurthy and Vijay Shenoy. The authors acknowledge DST, Government of India (Nano mission) for funding under project no.

DST/NM/TUE/QM-10/2019 (C)/7. MG acknowledges CSIR, India, for the senior research fellowship [grant no. 09/575 (0131) 2020-EMR-I]. BM and SB acknowledge Max Planck Partner group Grant at ICTS, Swarna Jayanti fellowship grant of SERB-DST (India) Grant No. SB/SJF/2021-22/12 and the Department of Atomic Energy, Government of India under Project No. RTI4001. SB acknowledges adjunct fellow program at SNBNCBS, Kolkata for hospitality. T.S.-D. acknowledges JC Bose National Fellowship (Grant No. JCB/2020/000004) for funding.

-
- [1] G. Cao and L. E. Delong, *Frontiers of 4D-and 5D-transition Metal Oxides* (World Scientific, 2013).
- [2] W. Witczak-Krempa, G. Chen, Y. B. Kim, and L. Balents, Correlated quantum phenomena in the strong spin-orbit regime, [arXiv preprint arXiv:1305.2193](#) (2013).
- [3] T. Takayama, J. Chaloupka, A. Smerald, G. Khaliullin, and H. Takagi, Spin-orbit-entangled electronic phases in 4d and 5d transition-metal compounds, *Journal of the Physical Society of Japan* **90**, 062001 (2021).
- [4] X. Wan, A. M. Turner, A. Vishwanath, and S. Y. Savrasov, Topological semimetal and fermi-arc surface states in the electronic structure of pyrochlore iridates, *Physical Review B* **83**, 205101 (2011).
- [5] M. Z. Hasan and C. L. Kane, Colloquium: Topological insulators, *Rev. Mod. Phys.* **82**, 3045 (2010).
- [6] X.-L. Qi and S.-C. Zhang, Topological insulators and superconductors, *Rev. Mod. Phys.* **83**, 1057 (2011).
- [7] Y. Chen, J. G. Analytis, J.-H. Chu, Z. Liu, S.-K. Mo, X.-L. Qi, H. Zhang, D. Lu, X. Dai, Z. Fang, *et al.*, Experimental realization of a three-dimensional topological insulator, Bi₂Te₃, *Science* **325**, 178 (2009).
- [8] J. Romhányi, L. Balents, and G. Jackeli, Spin-orbit dimers and noncollinear phases in d^1 cubic double perovskites, *Phys. Rev. Lett.* **118**, 217202 (2017).
- [9] G. Jackeli and G. Khaliullin, Mott insulators in the strong spin-orbit coupling limit: From Heisenberg to a quantum compass and Kitaev models, *Phys. Rev. Lett.* **102**, 017205 (2009).
- [10] G. Chen, R. Pereira, and L. Balents, Exotic phases induced by strong spin-orbit coupling in ordered double perovskites, *Phys. Rev. B* **82**, 174440 (2010).
- [11] C. Broholm, R. Cava, S. Kivelson, D. Nocera, M. Norman, and T. Senthil, Quantum spin liquids, *Science* **367**, eaay0668 (2020).
- [12] J. Knolle and R. Moessner, A field guide to spin liquids, *Annual Review of Condensed Matter Physics* **10**, 451 (2019).
- [13] H. Takagi, T. Takayama, G. Jackeli, G. Khaliullin, and S. E. Nagler, Concept and realization of Kitaev quantum spin liquids, *Nature Reviews Physics* **1**, 264 (2019).
- [14] B. J. Kim, H. Jin, S. J. Moon, J.-Y. Kim, B.-G. Park, C. S. Leem, J. Yu, T. W. Noh, C. Kim, S.-J. Oh, J.-H. Park, V. Durairaj, G. Cao, and E. Rotenberg, Novel $J_{\text{eff}} = 1/2$ mott state induced by relativistic spin-orbit coupling in Sr₂IrO₄, *Phys. Rev. Lett.* **101**, 076402 (2008).
- [15] B. Kim, H. Ohsumi, T. Komesu, S. Sakai, T. Morita, H. Takagi, and T.-h. Arima, Phase-sensitive observation of a spin-orbital mott state in Sr₂IrO₄, *Science* **323**, 1329 (2009).
- [16] J. Kim, D. Casa, M. Upton, T. Gog, Y.-J. Kim, J. Mitchell, M. Van Veenendaal, M. Daghofer, J. Van Den Brink, G. Khaliullin, *et al.*, Magnetic excitation spectra of Sr₂IrO₄ probed by resonant inelastic x-ray scattering: establishing links to cuprate superconductors, *Physical Review Letters* **108**, 177003 (2012).
- [17] M. A. McGuire, Crystal and magnetic structures in layered, transition metal dihalides and trihalides, *Crystals* **7**, 10.3390/cryst7050121 (2017).
- [18] M. G. Yamada, M. Oshikawa, and G. Jackeli, Emergent SU(4) symmetry in α -ZrCl₃ and crystalline spin-orbital liquids, *Phys. Rev. Lett.* **121**, 097201 (2018).
- [19] B. Mondal, V. B. Shenoy, and S. Bhattacharjee, Emergent SU(8) dirac semimetal and novel proximate phases of spin-orbit coupled fermions on a honeycomb lattice, [arXiv preprint arXiv:2304.07223](#) (2023).
- [20] J. Kanamori, Superexchange interaction and symmetry properties of electron orbitals, *Journal of Physics and Chemistry of Solids* **10**, 87 (1959).
- [21] C. L. Kane and E. J. Mele, Quantum spin hall effect in graphene, *Phys. Rev. Lett.* **95**, 226801 (2005).
- [22] T. Senthil, Symmetry-protected topological phases of quantum matter, *Annual Review of Condensed Matter Physics* **6**, 299 (2015).
- [23] The supplementary material contains additional information on transformation of basis, derivation of hamiltonian for X and Y bonds, evolution of band structure in $\tau_m - \tilde{\lambda}$ phase diagram, discussion on gapped phases, and dft computed magnetic ground states, .
- [24] P. E. Blöchl, Projector augmented-wave method, *Phys. Rev. B* **50**, 17953 (1994).
- [25] A. Tackett, N. Holzwarth, and G. Matthews, A projector augmented wave (PAW) code for electronic structure calculations, part II: pwpaw for periodic solids in a plane wave basis, *Computer Physics Communications* **135**, 348 (2001).
- [26] J. Paier, R. Hirschl, M. Marsman, and G. Kresse, The Perdew–Burke–Ernzerhof exchange–correlation functional applied to the G2-1 test set using a plane-wave basis set, *The Journal of Chemical Physics* **122**, 234102 (2005).
- [27] G. Kresse and J. Hafner, Ab initio molecular dynamics for liquid metals, *Physical review B* **47**, 558 (1993).
- [28] E. Eliav, U. Kaldor, and Y. Ishikawa, Open-shell relativistic coupled-cluster method with Dirac-Fock-Breit

- wave functions: Energies of the gold atom and its cation, *Physical Review A* **49**, 1724 (1994).
- [29] G. Kresse and D. Joubert, From ultrasoft pseudopotentials to the projector augmented-wave method, *Physical review b* **59**, 1758 (1999).
- [30] J. P. Perdew, K. Burke, and M. Ernzerhof, Generalized gradient approximation made simple, *Physical review letters* **77**, 3865 (1996).
- [31] S. L. Dudarev, G. A. Botton, S. Y. Savrasov, C. Humphreys, and A. P. Sutton, Electron-energy-loss spectra and the structural stability of nickel oxide: An LSDA+ U study, *Physical Review B* **57**, 1505 (1998).
- [32] S. Grimme, Semiempirical gga-type density functional constructed with a long-range dispersion correction, *Journal of computational chemistry* **27**, 1787 (2006).
- [33] O. K. Andersen and O. Jepsen, Explicit, first-principles tight-binding theory, *Physical Review Letters* **53**, 2571 (1984).
- [34] O. Andersen and T. Saha-Dasgupta, Muffin-tin orbitals of arbitrary order, *Physical Review B* **62**, R16219 (2000).
- [35] S. Troyanov, E. Snigireva, and V. Rybakov, An X-ray structural investigation of the phase transition in α -TiCl₃, *Russian journal of inorganic chemistry* **36**, 634 (1991).
- [36] G. Allegra, Il calcolo dell'intensità di diffrazione dei raggi x da parte di strutture denotanti disordine monodimensionale: Iii-studio strutturale di due diverse modificazioni cristalline del tiCl₃ che presentano disordine monodimensionale, *Il Nuovo Cimento* (1955-1965) **23**, 502 (1962).
- [37] The in-plane lattice constant of TiCl₃ in AAA, ABA, ABC is found to vary between 6.14 Å to 6.153 Å, while the inter-layer separation is found to vary between 5.850 Å to 5.866 Å.
- [38] T. R. Devidas, N. V. C. Shekar, C. S. Sundar, P. Chithaiah, Y. A. Sorb, V. S. Bhadrani, N. Chandrabhas, K. Pal, U. V. Waghmare, and C. N. R. Rao, Pressure-induced structural changes and insulator-metal transition in layered bismuth triiodide, BiI₃: a combined experimental and theoretical study, *Journal of Physics: Condensed Matter* **26**, 275502 (2014).
- [39] J. Ketelaar, C. MacGillavry, and P. Renes, The crystal structure of aluminium chloride, *Recueil des Travaux Chimiques des Pays-Bas* **66**, 501 (1947).
- [40] S. Troyanov, V. Ionov, and V. Rybakov, The synthesis and crystal structures of TiBr₄, TiBr₃, and Ti(AlBr₄)₂, *Žurnal neorganičeskoj himii* **35**, 882 (1990).
- [41] B. Swaroop and S. Flengas, Crystal structure of zirconium trichloride, *Canadian Journal of Physics* **42**, 1886 (1964).
- [42] J. Daintith, *A dictionary of chemistry* (Oxford University Press, 2008).
- [43] P. A. Maksimov, A. V. Ushakov, Z. V. Pchelkina, Y. Li, S. M. Winter, and S. V. Streltsov, Ab initio guided minimal model for the “Kitaev” material BaCo₂(AsO₄)₂: Importance of direct hopping, third-neighbor exchange, and quantum fluctuations, *Phys. Rev. B* **106**, 165131 (2022).
- [44] D. Guterding, H. O. Jeschke, and R. Valentí, Prospect of quantum anomalous hall and quantum spin hall effect in doped kagome lattice mott insulators, *Scientific reports* **6**, 1 (2016).
- [45] N. Goldman, D. F. Urban, and D. Bercioux, Topological phases for fermionic cold atoms on the Lieb lattice, *Phys. Rev. A* **83**, 063601 (2011).
- [46] I. Lifshitz *et al.*, Anomalies of electron characteristics of a metal in the high pressure region, *Sov. Phys. JETP* **11**, 1130 (1960).
- [47] G. Volovik, Topological Lifshitz transitions, *Low Temperature Physics* **43**, 47 (2017).
- [48] L. Fu and C. L. Kane, Topological insulators with inversion symmetry, *Phys. Rev. B* **76**, 045302 (2007).
- [49] Y. Yamaji, T. Misawa, and M. Imada, Quantum and topological criticalities of Lifshitz transition in two-dimensional correlated electron systems, *Journal of the Physical Society of Japan* **75**, 094719 (2006).
- [50] M. Rodney, H. F. Song, S.-S. Lee, K. Le Hur, and E. S. Sørensen, Scaling of entanglement entropy across Lifshitz transitions, *Phys. Rev. B* **87**, 115132 (2013).
- [51] V. Sunko, E. Abarca Morales, I. Marković, M. E. Barber, D. Milosavljević, F. Mazzola, D. A. Sokolov, N. Kikugawa, C. Cacho, P. Dudin, *et al.*, Direct observation of a uniaxial stress-driven Lifshitz transition in Sr₂RuO₄, *npj Quantum Materials* **4**, 46 (2019).
- [52] H.-Y. Kee, E. H. Kim, and C.-H. Chung, Signatures of an electronic nematic phase at the isotropic-nematic phase transition, *Phys. Rev. B* **68**, 245109 (2003).
- [53] S. T. Carr, J. Quintanilla, and J. J. Betouras, Lifshitz transitions and crystallization of fully polarized dipolar fermions in an anisotropic two-dimensional lattice, *Phys. Rev. B* **82**, 045110 (2010).
- [54] S. Ghamari, S.-S. Lee, and C. Kallin, Renormalization group analysis of a neck-narrowing Lifshitz transition in the presence of weak short-range interactions in two dimensions, *Phys. Rev. B* **92**, 085112 (2015).
- [55] A. Kapustin, T. McKinney, and I. Z. Rothstein, Wilsonian effective field theory of two-dimensional Van Hove singularities, *Phys. Rev. B* **98**, 035122 (2018).
- [56] V. V. Gapontsev, D. D. Gazizova, and S. V. Streltsov, Dimerization in α -TiCl₃ and α -TiBr₃: the dft study, *Journal of Physics: Condensed Matter* **33**, 495803 (2021).
- [57] P. Fulde and R. A. Ferrell, Superconductivity in a strong spin-exchange field, *Phys. Rev.* **135**, A550 (1964).
- [58] A. Larkin and Y. N. Ovchinnikov, Nonuniform state of superconductors, *Zh. Eksperim. i Teor. Fiz.* **47** (1964).

Supplemental Material: Ab-initio Insights on the Fermiology of d^1 Transition metals
in Honeycomb lattice : Hierarchy of hopping pathways and spin-orbit coupling

arXiv:2308.08526v1 [cond-mat.str-el] 16 Aug 2023

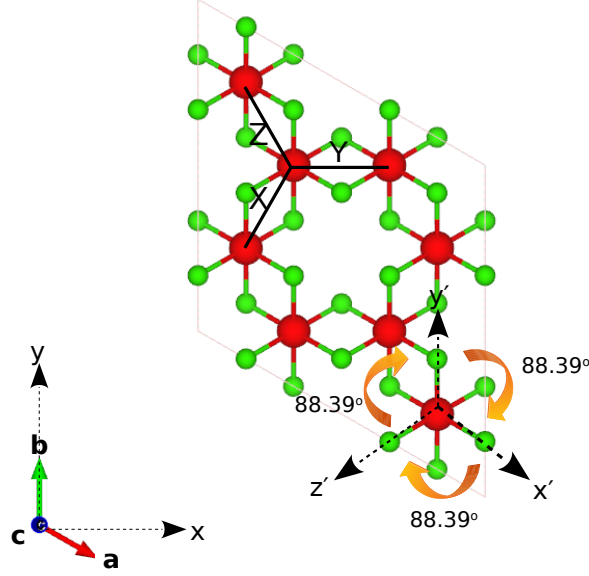


FIG. 1. Global and local coordinate systems denoted by x, y, z , and x', y', z' , respectively. Red and green balls represent to metal (M) and halide (X) ions, respectively. A metal ion is connected to its nearest neighbours via X,Y, and Z bonds, also marked in the figure.

I. TRANSFORMATION OF BASIS: GLOBAL TO HALIDE-BASED, PRIMED COORDINATE SYSTEM

In the global coordinate system, the x -axis points in the direction making 30° with \mathbf{a} , y pointing along \mathbf{b} , and z along \mathbf{c} . A Local octahedral coordinate system is defined by x', y' , and z' axis, where the corresponding x -axis, y -axis, and z -axis point along the bonds M-X as shown in the Fig.(1).

The transformation matrix rotating the global coordinate system to the local coordinate system, for ZrCl_3 , is given by

$$x' = (-0.7089)x + (0.4051)y + (-0.5772)z$$

$$y' = (0.0034)x + (-0.8165)y + (-0.5772)z$$

$$z' = (-0.7052)x + (-0.4112)y + (0.5774)z$$

It is to be noted that due to trigonal distortion, the M-X bonds are not orthogonal to each other in the octahedron but have a mutual angle of 88.39° . Thus the above transformation matrix aligns the x', y' , and z' axis, approximately, along the M-X bonds shown in the Fig.(1). The rotation of the coordinate system, given above, gets reflected on d-orbitals via the transformation matrix as

$$d_{x'y'} = (0.5802)d_{xy} + (0.2374)d_{yz} + (0.5772)d_{z^2} + (0.4072)d_{xz} + (0.3283)d_{x^2-y^2}$$

$$d_{y'z'} = (0.5744)d_{xy} + (-0.2340)d_{yz} + (-0.5774)d_{z^2} + (0.4091)d_{xz} + (-0.3382)d_{x^2-y^2}$$

$$d_{z'^2} = (0.5023)d_{xy} + (-0.4113)d_{yz} + (0.0001)d_{z^2} + (-0.7053)d_{xz} + (0.2842)d_{x^2-y^2}$$

$$d_{x'z'} = (0.0058)d_{xy} + (0.4713)d_{yz} + (-0.5774)d_{z^2} + (-0.0022)d_{xz} + (0.6666)d_{x^2-y^2}$$

$$d_{x'^2-y'^2} = (-0.2843)d_{xy} + (-0.7052)d_{yz} + (-0.0000)d_{z^2} + (0.4112)d_{xz} + (0.5025)d_{x^2-y^2}$$

II. DERIVATION OF h_X, h_Y FROM h_Z

Since the Hamiltonian, given in Eq. 1 of the main text, is symmetric under the action of C_3 rotation, the hopping matrices on the Y and the X M-M bonds can be obtained from that on the Z -bonds, by the transformation given by,

$$h_X = \mathcal{R}_3^\dagger h_Z \mathcal{R}_3 \quad (1)$$

$$h_Y = \mathcal{R}_3^\dagger h_X \mathcal{R}_3. \quad (2)$$

Here, \mathcal{R}_3 is a 3×3 unitary operator that implements C_3 rotation about an axis perpendicular to the plane of the honeycomb lattice, on the t_{2g} orbitals and is given by

$$\mathcal{R}_3 = \begin{pmatrix} 0 & 1 & 0 \\ 0 & 0 & 1 \\ 1 & 0 & 0 \end{pmatrix}. \quad (3)$$

III. EVOLUTION OF THE BAND STRUCTURES IN τ_m - $\tilde{\lambda}$ PHASE DIAGRAM

1. The $\tilde{\lambda} = 0$ line

Fig 2 shows the band structures at different points on the $\lambda = 0$ line of the τ_m - $\tilde{\lambda}$ phase diagram in Fig. 6a of the main text. At $\tau_m = 0$ on this line, there are two flat bands, each of which are six-fold degenerate. As τ_m is increased, six 2-fold degenerate bands appear. Finally at $\tau_m = 1$, there are four bands with the lowest and the top bands being 2-fold and the rest being 4-fold degenerate.

2. The $\tau_m = 0$ line

The energy spectrum along the $\tau_m = 0$ line is shown in Fig. 3. The band structure for $\tilde{\lambda} = 0$ is (cf. the $\tilde{\lambda} = 0, \tau_m = 0$ line in Fig. 2) has two six-fold degenerate bands. As $\tilde{\lambda}$ is increased, six 2-fold degenerate bands appear, two of them being completely flat.

3. The $\tau_m = 1$ line

The evolution of energy spectrum along the $\tau_m = 1$ line is shown in Fig. 4. The band structure for $\tilde{\lambda} = 0$ on this line is has four bands (cf. $\tilde{\lambda} = 0, \tau_m = 1$ in Fig. 2). For large values of $\tilde{\lambda}$, the $J = 3/2$ and the $J = 1/2$ bands are separated. For $\tilde{\lambda} = 20, \tau_m = 1$, only the lowest $J = 3/2$ bands are shown.

IV. PROPERTIES OF GAPPED PHASES

1. $SU(8)$ Dirac theory at the P_3 point

At P_3 point of the phase diagram in Fig. 6 and Fig. 11 of the main text, the low-energy effective theory is described by massless Dirac fermions with internal $SU(8)$ symmetry. Below we sketch the derivation of the Dirac theory. The details can be found in Ref. [1].

At the P_3 point, the form of the Hamiltonian in Eq. 5 of the main text, when projected to the low-energy $J = 3/2$ orbitals, is given by

$$\mathcal{H}_{P_3} = -\frac{\mathcal{E}}{\sqrt{3}} \left(\sum_{\langle ij \rangle \in X\text{-bonds}} \psi_i^\dagger U_X \psi_j + \sum_{\langle ij \rangle \in Y\text{-bonds}} \psi_i^\dagger U_Y \psi_j + \sum_{\langle ij \rangle \in Z\text{-bonds}} \psi_i^\dagger U_Z \psi_j \right). \quad (4)$$

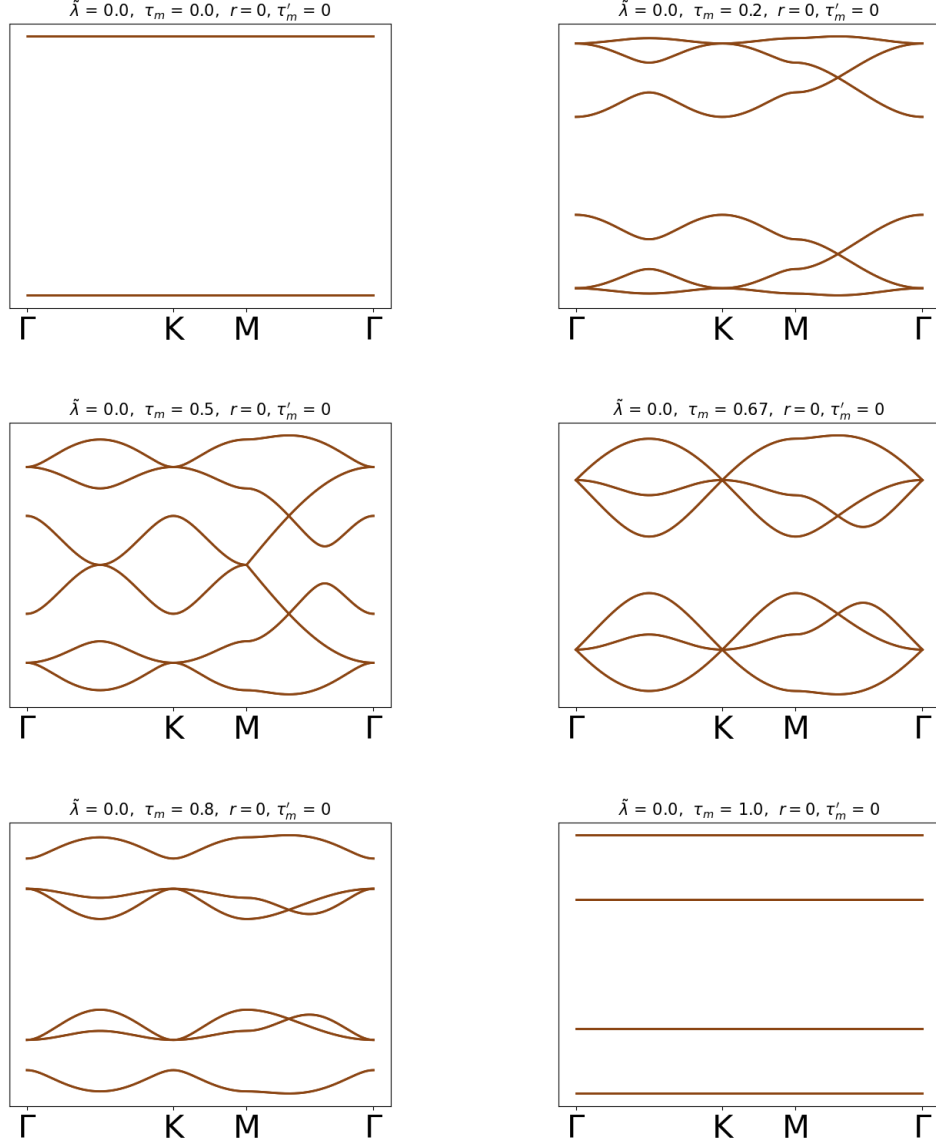


FIG. 2. Evolution of band structure along the $\tilde{\lambda} = 0$ line of the phase diagram in Fig. 6 of the main text.

Here, ψ_i is a 4-component annihilation operator corresponding to the four $J = 3/2$ orbitals at the site i . The U_X, U_Y, U_Z are 4×4 Hermitian matrices, which are given by

$$U_X = -\rho \Sigma_1 \quad (5)$$

$$U_Y = -\rho \Sigma_2 \quad (6)$$

$$U_Z = -\rho \Sigma_3. \quad (7)$$

Here, $\rho = +1$ for the phase diagram in Fig. 6a and $\rho = -1$ for Fig. 11. The Σ_i (for $i = 1, \dots, 15$) are the 15 linearly independent 4×4 traceless Hermitian matrices which are given in Appendix. C of Ref. [1], which are essentially the generators of a $SU(4)$ group. Note, the Hamiltonian in Eq. 4 has an internal $SU(4)$ symmetry[2].

Projecting this Hamiltonian in Eq 4 to the two lowest two bands which touch linearly at the Fermi energy, we get the $SU(8)$ symmetric Dirac Hamiltonian given by

$$\mathcal{H}_{Dirac} = \rho v_F \int d^2 \mathbf{r} \chi^\dagger(\mathbf{r}) (-i\alpha_1 \partial_1 - i\alpha_2 \partial_2) \chi(\mathbf{r}), \quad (8)$$

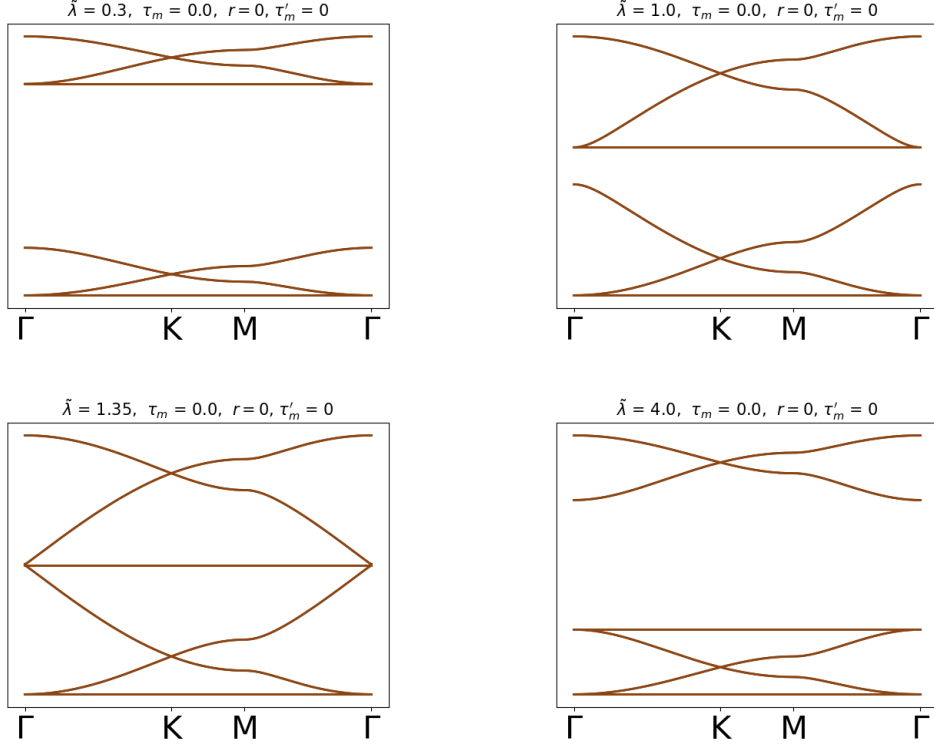


FIG. 3. Evolution of band structure along the $\tau_m = 0$ line of the phase diagram in Fig. 6 of the main text.

with

$$\alpha_1 = \Sigma_0 \otimes \tau_3 \otimes \sigma_1 \quad (9)$$

$$\alpha_2 = \Sigma_0 \otimes \tau_0 \otimes \sigma_2. \quad (10)$$

Here, v_F is the Fermi velocity, which is related to the gradient of the linearly dispersing bands at the Dirac points. $\chi(\mathbf{r})$ is the 16-component Dirac spinor at the position \mathbf{r} . Both τ_i and σ_i (for $i = 1, 2, 3$) are the Pauli matrices with τ_0 and σ_0 being the 2×2 identity matrix. The generators of the SU(8) symmetry are the set of 63 matrices given by

$$\{\Sigma_0, \Sigma_i\} \otimes \{\tau_3\sigma_0, \tau_1\sigma_2, \tau_2\sigma_2\}, \quad \Sigma_i \otimes \tau_0\sigma_0 \quad (11)$$

for $i = 1, \dots, 15$.

2. The topological gapped phase

On moving left from the P_3 point along the $\tilde{\lambda} = \infty$ line by reducing the value of τ_m from 1, the effective hopping Hamiltonian in the $J = 3/2$ sector is given by

$$\mathcal{H}_{top} = -\frac{\mathcal{E}}{\sqrt{3}} \sum_{\langle ij \rangle} \psi_i^\dagger \tilde{H}_{ij} \psi_j, \quad (12)$$

with

$$\begin{aligned} \tilde{H}_X &= U_X + (1 - \tau_m) \left[\frac{1}{3} \Sigma_0 + \frac{1}{6} \left(-\sqrt{3} \Sigma_4 + \Sigma_5 \right) \right] \\ \tilde{H}_Y &= U_Y + (1 - \tau_m) \left[\frac{1}{3} \Sigma_0 + \frac{1}{6} \left(\sqrt{3} \Sigma_4 + \Sigma_5 \right) \right] \\ \tilde{H}_Z &= U_Z + (1 - \tau_m) \left[\frac{1}{3} \Sigma_0 - \frac{1}{3} \Sigma_5 \right]. \end{aligned} \quad (13)$$

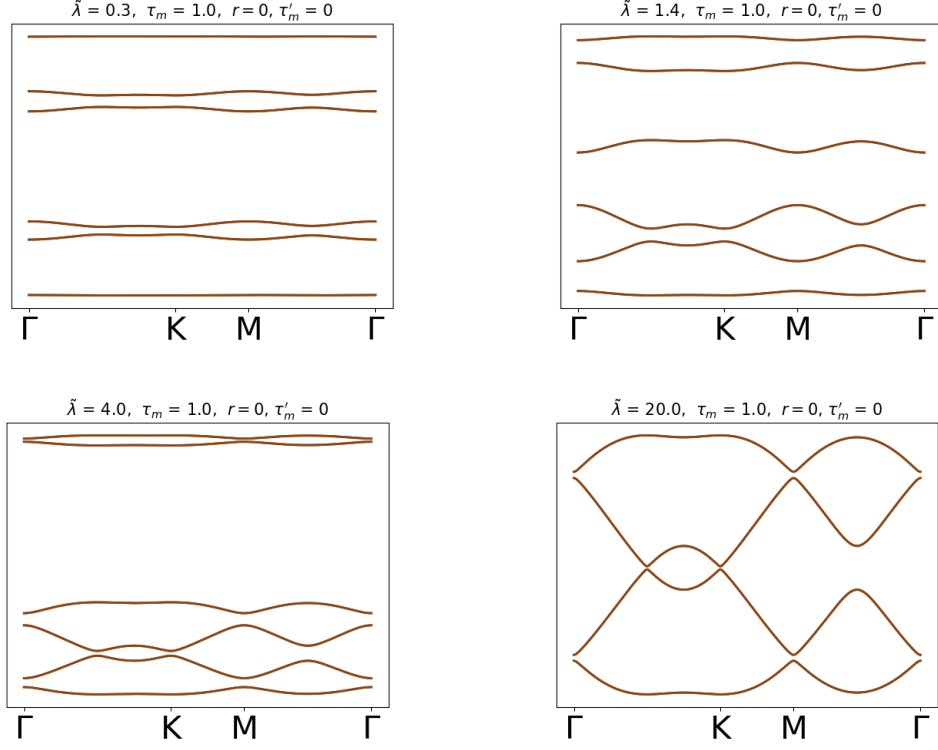


FIG. 4. Band structures along the $\tau_m = 1$ line of the phase diagram in Fig. 6 of the main text. All the bands are 2-fold degenerate. For $\tilde{\lambda} = 20$, only four bands are shown leaving out higher energy $J = 1/2$ orbitals.

On projecting this Hamiltonian to the lowest two bands, we get the following effective low-energy Hamiltonian

$$\mathcal{H}_{top} = \mathcal{H}_{Dirac} + (1 - \tau_m)\mathcal{H}_m^{(1)} + (1 - \tau_m)\mathcal{H}'. \quad (14)$$

Here, \mathcal{H}_{Dirac} is given by Eq. 8. The $\mathcal{H}_m^{(1)}$ and \mathcal{H}' are given by

$$\mathcal{H}_m^{(1)} = \int d^2\mathbf{r} \chi^\dagger (\Sigma_1\tau_1\sigma_0 - \Sigma_2\tau_2\sigma_1 + \Sigma_3\tau_0\sigma_3) \chi, \quad (15)$$

and

$$\mathcal{H}' = \chi^\dagger (-i\partial_x\delta\alpha_x - i\partial_y\delta\alpha_y) \chi, \quad (16)$$

with

$$\delta\alpha_x = -\Sigma_3\tau_3\sigma_1 + \frac{1}{\sqrt{3}}\Sigma_{35}\tau_0\sigma_0 + \frac{\sqrt{3}}{\sqrt{2}}\Sigma_{35}\tau_0\sigma_3 \quad (17)$$

and

$$\begin{aligned} \delta\alpha_y = & \frac{1}{\sqrt{6}}(\Sigma_1\tau_1\sigma_2 - \Sigma_2\tau_2\sigma_2) + \frac{\sqrt{3}}{2\sqrt{2}}(\Sigma_{14}\tau_1\sigma_1 - \Sigma_{24}\tau_2\sigma_1) - \frac{1}{2}(\Sigma_{14}\tau_2\sigma_3 - \Sigma_{24}\tau_1\sigma_3) - \frac{1}{2\sqrt{2}}(\Sigma_{15}\tau_1\sigma_1 + \Sigma_{25}\tau_2\sigma_1) \\ & + \frac{1}{2\sqrt{3}}(\Sigma_{15}\tau_2\sigma_3 + \Sigma_{25}\tau_1\sigma_3) \end{aligned} \quad (18)$$

The term $\mathcal{H}_m^{(1)}$ is the ferro-quadrupolar quantum Hall mass listed in Ref.[1] whose edge modes are protected by the time reversal (TR) symmetry. Thus, the phase obtained by moving left from the P_3 point in the phase diagram in Fig. 6a is a Z_2 topological insulator. The presence of \mathcal{H}' does not change the topological character of this phase since this term does not break the TR symmetry and can be tuned to zero without closing the fermionic energy gap.

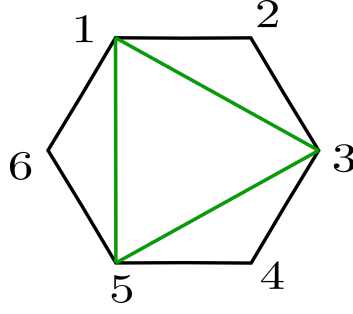


FIG. 5. A single hexagon of a honeycomb lattice showing the three kinds of next nearest neighbour bonds (green bonds). The six sites are labelled with integers from 1 to 6.

3. The non-topological phase

On moving down vertically from the P_3 point along the $\tau_m = 1$ line, we encounter the non-topological gapped phase. This can be understood by doing a similar analysis as done for the previous gapped phase. For very large values of $\tilde{\lambda}$ and $\tau_m = 1$, the effective Hamiltonian is given by

$$\mathcal{H}_{non-top} = -\mathcal{E} \left(\sum_{\langle ij \rangle} \psi_i^\dagger U_{ij} \psi_j + \frac{1}{\lambda} \sum_{\langle\langle ij \rangle\rangle} \psi_i^\dagger \tilde{H}_{ij} \psi_j + h.c. \right) \quad (19)$$

Where the U_{ij} are the matrices defined in Eq. 5 and \tilde{H}_{ij} are the hopping matrices on the next-nearest(NNN) bonds of the lattice. On the three kinds of NNN bonds shown in Fig 5, the \tilde{H}_{ij} matrices are given by

$$\begin{aligned} \tilde{H}_{13} &= -\frac{1}{2\sqrt{3}}\Sigma_1 + \frac{i}{6} \left(-\Sigma_{14} - \sqrt{3}\Sigma_{15} - \Sigma_{23} \right) \\ \tilde{H}_{35} &= -\frac{1}{2\sqrt{3}}\Sigma_2 + \frac{i}{6} \left(\Sigma_{13} - \Sigma_{24} + \sqrt{3}\Sigma_{25} \right) \\ \tilde{H}_{51} &= -\frac{1}{2\sqrt{3}}\Sigma_3 + \frac{i}{6} \left(-\Sigma_{12} + 2\Sigma_{34} \right) \end{aligned} \quad (20)$$

On projecting this Hamiltonian to the lowest two bands near the Dirac points, we get the following low-energy theory

$$\mathcal{H}_{non-top} = \mathcal{H}_{Dirac} + \frac{1}{\lambda} \mathcal{H}_m^{(2)} + \frac{1}{\lambda} \mathcal{H}'' \quad (21)$$

Here, \mathcal{H}_{Dirac} is the SU(8) symmetric Dirac Hamiltonian. The $\mathcal{H}_m^{(2)}$ is given by

$$\mathcal{H}_m^{(2)} = \int d^2x \chi^\dagger \Sigma_{45} \tau_3 \sigma_3 \chi \quad (22)$$

The $\mathcal{H}_m^{(2)}$ is one of the topological masses proximate to the SU(8) Dirac semi-metal. The edge modes of this topological symmetry is protected by a U(1) symmetry which is generated by Σ_{45} . But the term \mathcal{H}'' breaks this U(1) symmetry and destroys the edge modes. This explains the existence of the non-topological phase in the phase diagram.

4. Phase transition lines in τ_m - $\tilde{\lambda}$ plane with $\rho = \pm 1$

On the phase transition line, the P_1P_3 line, between the two gapped phases shown in Fig. 6a of the main text, the lowest two bands touch each other linearly at the Γ point as shown in inset VI of the same figure. One can find the low-energy theory for this point of the phase diagram by projecting the Hamiltonian to the two lowest band that touch at the Γ point. The resultant theory is given by

$$\mathcal{H}_\Gamma = -iv_F \int d^2x \chi_\Gamma^\dagger (\tau_3 \sigma_1 \partial_1 + \tau_0 \sigma_2 \partial_2) \chi_\Gamma \quad (23)$$

Here, χ_Γ is a 4-component spinor which comes from the two-fold degenerate Dirac cone at the Γ point. This Hamiltonian has an emergent SU(2) symmetry which is generated by $\{\tau_3\sigma_0, \tau_1\sigma_2, \tau_2\sigma_2\}/2$.

Similarly, on the P_3P_{14} line of the phase of Fig. 11, the lower two bands touch each other linearly at the three M points. The low-energy theory at any point on this line is given by

$$\mathcal{H}_M = i \int d^2x \chi_M^\dagger (v_x \mathbb{I}_{3 \times 3} \otimes \tau_3 \sigma_1 \partial_1 + v_y \mathbb{I}_{3 \times 3} \otimes \tau_0 \sigma_2 \partial_2) \chi_M. \quad (24)$$

Here, χ_M is a 12-component spinor that comes from the three two-fold degenerate Dirac cones at the three M points. v_x and v_y are the Fermi velocities along the two Cartesian directions. The values of these two numbers depend on the position on the phase transition line. $\mathbb{I}_{3 \times 3}$ is the three dimensional identity matrix that acts on the space of the three M valleys. This Hamiltonian has an internal SU(6) symmetry which are generated by the set of Hermitian matrices given by

$$\{\mathbb{I}_{3 \times 3}, \Lambda_i\} \otimes \{\tau_3\sigma_0, \tau_1\sigma_2, \tau_2\sigma_2\}, \quad \Lambda_i \otimes \tau_0\sigma_0 \quad (25)$$

where the Λ_i are the eight 3×3 Gell-Mann matrices that generate an SU(3).

V. DFT COMPUTED MAGNETIC GROUND STATES

As discussed in main text, one of the possible consequence of inclusion of Coulomb correlation is to stabilize magnetism. To identify the magnetic ground states of the undimerized MX_3 compounds, DFT total energies for magnetic configurations, e.g non-magnetic(NM), ferromagnetic(FM), Neel-antiferromagnetic (AFM), zigzag-AFM (ZAFM), and stripe-AFM (SAFM) were calculated within the GGA+U+SOC formulation to take into account of the Coulomb correlation in a mean-field way along with SOC, and compared. The Coulomb correlation is modeled through supplemented Hubbard U correction and the Hund's coupling J to account for the multi-orbital nature of the problem.

The calculated spin and orbital magnetic moments of the nine compounds are tabulated in Table I. As expected, the orbital moment shows an increasing trend in moving from Ti to Zr to Hf compounds, while the spin moment shows an decreasing trend. This is justified by increase of SOC in moving 3d to 4d to 5d transition metal series, and extended nature of the wavefunction in moving from 3d to 4d/5d.

The computed magnetic phase diagram, is shown in Fig 6 in the plane of compounds versus choice of (U-J) parameter. Marked are the lowest energy magnetic state according to DFT total energy, their conducting properties estimated from density of states plots. The metal-insulator transitions as well as magnetic transitions are marked by boundaries.

First of all, we notice in a large part of the phase diagram, the FM state is stabilized, with the exception of SAFM or ZAFM phases at large value of (U-J) for Ti and Zr compounds. Although the (U-J) is varied over a large range in the plot, for the realistic estimates of U value for early transition metal like 3d Ti will be 3-4 eV, while 4d/5d Zr/Hf will be 1-2 eV. With estimated J value of 1 eV for 3d transition metal and 0.4 eV for 4d/5d transition metal, this amounts to (U-J) value of 2-3 eV for Ti compounds, and 0.6-1.6 eV for Zr/Hf compounds. With this choice, undimerized TiF_3 turns to be FM metal, while $\text{TiCl}_3/\text{TiBr}_3$ may exhibit stabilization of ZAFM phase. For 4d/5d Zr/Hf compounds, in undimerzed structure, the FM metallic phase wins over the AFM phases.

MX_3	Orbital Moment(μ_B)	Spin Moment(μ_B)
TiF ₃	-0.061	0.922
TiCl ₃	-0.003	0.938
TiBr ₃	-0.008	0.965
ZrF ₃	-0.044	0.722
ZrCl ₃	-0.034	0.661
ZrBr ₃	-0.026	0.674
HfF ₃	-0.132	0.806
HfCl ₃	-0.104	0.626
HfBr ₃	-0.111	0.728

TABLE I. Orbital and Spin Magnetic Moments on Metal(M) site for MX_3 , as calculated within GGA+U+SOC. (U-J) value was chosen to be 3 eV for Ti and 2 eV for Zr/Hf.

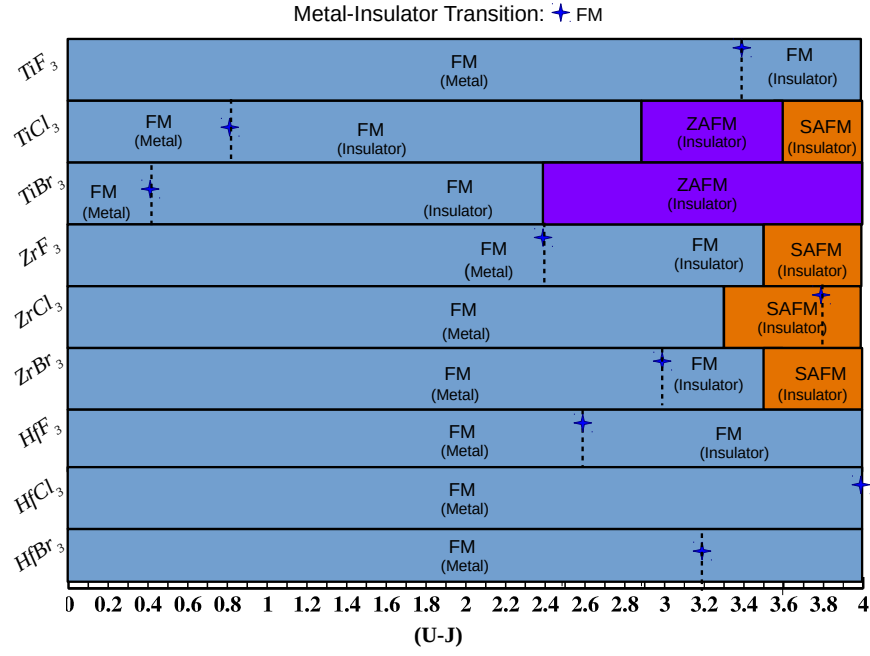


FIG. 6. Magnetic Ground states for MX_3 for various different choices of $(U-J)$ in eV.

-
- [1] B. Mondal, V. B. Shenoy, and S. Bhattacharjee, [arXiv preprint arXiv:2304.07223](#) (2023).
 [2] M. G. Yamada, M. Oshikawa, and G. Jackeli, [Physical Review Letters](#) **121**, 097201 (2018).